Supplementary Information

High-Flux and Anti-Fouling Membrane Distillation Membrane with VOC Capture Ability Enabled by ZIF-8

Dafei Sheng[1], Xinlin Li[1], Xin Huang[1], Dou Ma[1], Chao Sun[1], Yuhao Zhu[1], Xiaoqi Wang[2], Zhipeng Wang[3], Xiao Feng[1*], Shuang Zhao[1*] & Bo Wang[1*]

[1]Frontiers Science Center for High Energy Material, School of Chemistry and Chemical Engineering, Beijing Institute of Technology, Beijing 100081, P. R. China.

[2]PetroChina Research Institute of Petroleum Exploration & Development, Beijing 100083, P. R. China.

[3]State Key Laboratory of Applied Organic Chemistry, College of Chemistry and Chemical Engineering, Lanzhou Magnetic Resonance Center, Lanzhou University, Lanzhou, Gansu 730000, China.

*E-mail: fengxiao86@bit.edu.cn; shuangzhao@bit.edu.cn; bowang@bit.edu.cn

Table of Contents

Section 1. Supplementary Methods (1-3)

Section 2. Supplementary Figures (1-39)

Section 3. Supplementary Tables (1-19)

Section 4. Supplementary References (1-35)

Section 1. Supplementary Methods

Supplementary Method 1. Density functional theory (DFT)

The adsorption configurations of toluene in ZIF-8 were optimized by density functional theory (DFT) calculations performed with the CASTEP module (Materials Studio 2017 R2). The generalized gradient approximation (GGA) with Perdew–Burke–Ernzerhof (PBE) exchange-correlation was employed in all calculations. A semi-empirical addition of dispersive forces to conventional DFT was included in the calculation to account for van der Waals interactions. A cutoff energy of 544 eV and a 2×1×1 k-point mesh was found to be enough for the total energy to converge within 0.01 meV $atom^{-1}$. The structures and the atomic positions of MOFs were first fully optimized. Then the guest gas molecules were introduced in the channel pore, followed by a full structural relaxation. The equation for the calculation of binding energy is defined as BE = E(AB) – [E(A) + E(B)], where E(A) is the total energy of the adsorbate, E(B) is the total energy of the substrate, and E(AB) is the total energy of the adsorbate/substrate system in the equilibrium state. The structural transformation associated with toluene transport between the known energy minimum configurations was further calculated by relaxed scan calculations. In the scan calculations, the C atoms of toluene as well as the Zn atoms of ZIF-8 were held fixed, the other atoms were kept relaxed. The simulation parameters used in the relaxed scan calculations were identical to those in the energy minimization calculation.

Supplementary Method 2. Molecular dynamics (MD) simulation

Molecular dynamics simulation was performed to investigate the evaporation of water on ZIF-8 and SiO_2 surface at 70 ºC by using the GROMACS 2021.7 package[1]. The ZIF-8 (110) model was built with an area of 48.058 × 50.973 $Å^2$ in the surface plane and the force field parameters were taken from Li et al[2]. Water molecules adopted the SPCE model[3]. For the simulations, we have fixed the positions of Zn atoms in the ZIF-8 model or fixed ZIF-8, and 1000 free water molecules were placed on the ZIF-8 surface. 1000 free water molecules were placed on the SiO_2 surface with the sectional size of 33.368 × 34.842 $Å^2$, and the model and force field were obtained from Emami et al. work[4]. The SiO_2 model was fixed in the simulations. The Canonical Ensemble (NVT) was adopted to simulate the evaporation process. The simulation temperature was maintained at 343 K. The simulation lasted for at least 2 ns, the escaped water molecules reached an evaporation balance of less than 1 ns. The simulation results were visualized by using visual molecular dynamics (VMD)[5].

To investigate the evaporation of pure water, the molecular dynamics simulations were carried out using the Large Atomic/Molecular Massively Parallel Simulator (LAMMPS, version 2 Aug2023)[6]. 1000 free water molecules were placed on the surface of the bulk water layer with the sectional size of 48.058 × 50.973 $Å^2$, which is the same size as the ZIF-8 (110) surface. The bulk water layer was fixed in the simulations. Water molecules adopted the SPCE model[3]. The Canonical Ensemble (NVT) was adopted to simulate the evaporation process. The simulation temperature was maintained at 343 K. The simulation lasted 2 ns. In this work, the evaporation boundary condition is set at 5.0 Å above the water surface, and every water molecule reaching above it will be removed from the system. This setting has been used to evaluate the evaporation rate in previous work[7]. The simulation results were visualized by using visual molecular dynamics (VMD)[5].

Supplementary Method 3. Energy accounting

Energy balance is given by

$$H_1 = H_2 + Q_m + Q_0 + Q_v + W \quad (S1)$$

where H_1 is the internal energy of brine flowing into the system per unit time, H_2 is the internal energy of the brine flowing out of the system per unit time, Q_m is the heat loss per unit time membrane conduction, Q_0 is the amount of heat the system emits to the environment per unit time, Q_v includes the heat carried by transmembrane brine per unit time, the heat absorbed during evaporation, and the heat consumed in brine separation, and W is the work done by the water vapor in the system to the thin air outside the membrane through adiabatic expansion in unit time. We can write each term as follows:

$$H_1 = F\overline{H^0} + FC_p\left(T_1 - T_{ref}\right) \quad (S2)$$

$$H_2 = (F - JA_m)\overline{H^0} + (F - JA_m)C_P\left(T_2 - T_{ref}\right) \quad (S3)$$

$$Q_m = \frac{h_m(T_3 - T_4)A_m}{d_m} \quad (S4)$$

$$Q_0 = \frac{h_0\left[\frac{(T_1 + T_2)}{2} - T_5\right]A_0}{d_0} \quad (S5)$$

$$Q_v = JA_m\overline{H^0} + JA_m\Delta E + JA_mC_p\left[\frac{(T_1 + T_2)}{2} - T_{ref}\right] \quad (S6)$$

$$W = \frac{JA_mR(T_3 - T_4)}{(\gamma - 1)M_{H_2O}} \quad (S7)$$

The following parameters are involved in the energy accounting measurements.

F: Flow rate of salt water stream, which is fixed to be 4.957 g s^{-1}.

C_p: Heat capacity of 10 wt% salt water (3.67 J g^{-1} K^{-1}).

T_{ref}: Reference temperature, here taken to be T_{ref} = 0 °C.

$\overline{H^0}$: Internal energy passing through brine per unit time at 0 °C.

J: Water flux, L m^{-2} h^{-1}.

A_m: Membrane area (9×10^{-4} m^2).

d_m: Membrane thickness, m.

h_m: Thermal conductivity of the membrane, W m^{-1} K^{-1}.

h_0: Thermal conductivity of the module to count heat loss to the environment, W m^{-1} K^{-1}.

d_0: Membrane module thickness, m.

A_0: Membrane module area, m^2.

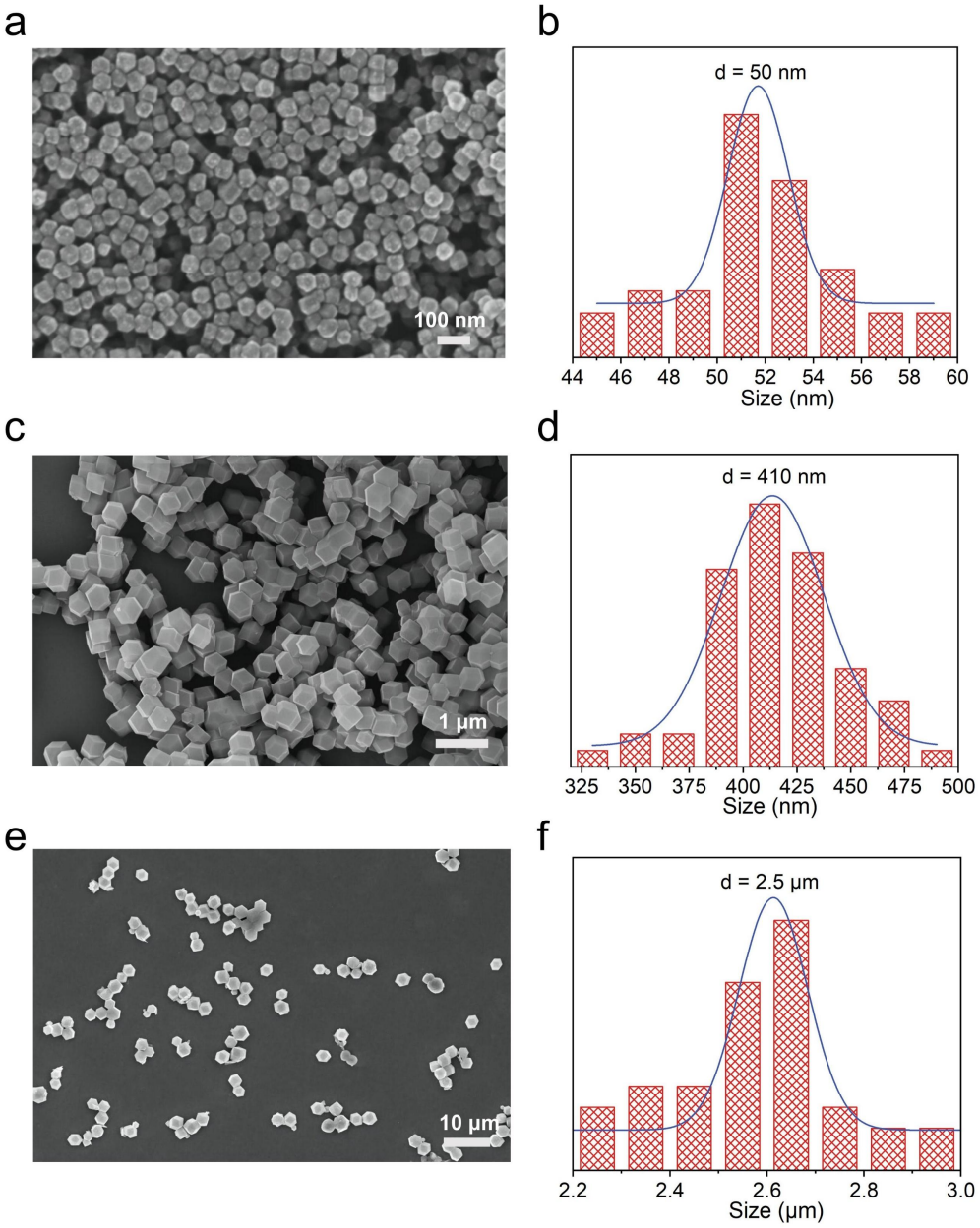
γ: The adiabatic coefficient of water vapor (1.3).

ΔE: The amount of energy required per unit mass of water to evaporate across membranes and separate salts, J g^{-1}.

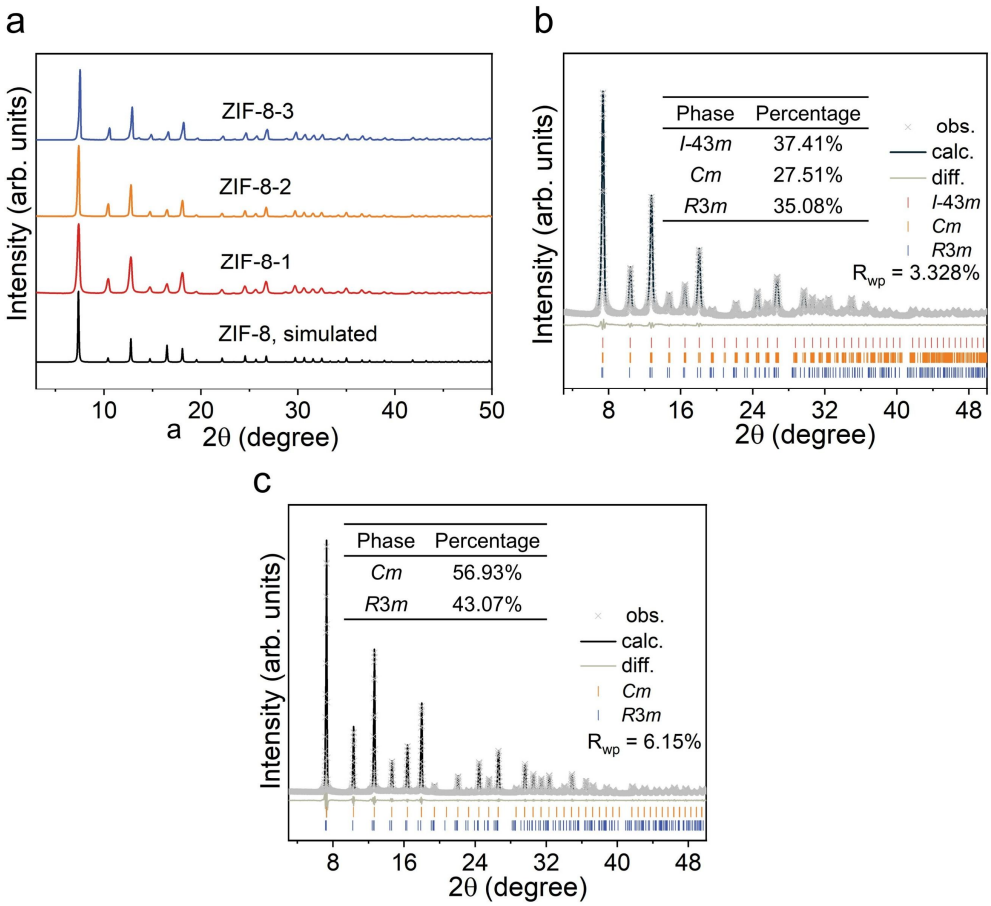
ΔE_{sys}: The system produces energy consumed per unit mass of water, J g^{-1}

$$\Delta E_{sys} = \frac{H_1 - H_2}{JA_m} \qquad (S8)$$

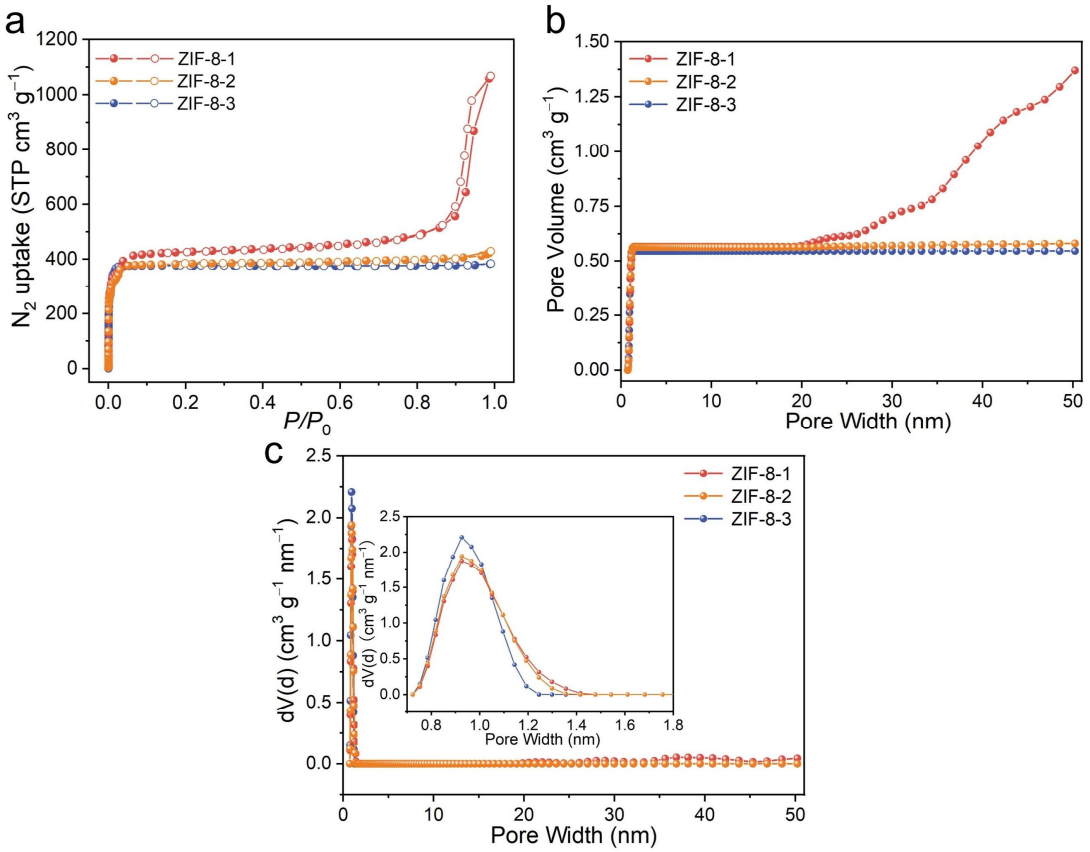
Section 2. Supplementary Figures



Supplementary Fig. 1. SEM morphology and particle size distributions of ZIF-8 samples. SEM image of ZIF-8-1 (a) and its particle size distribution (b); SEM image of ZIF-8-2 (c) with corresponding distribution (d); and SEM image of ZIF-8-3 (e) with its distribution (f).

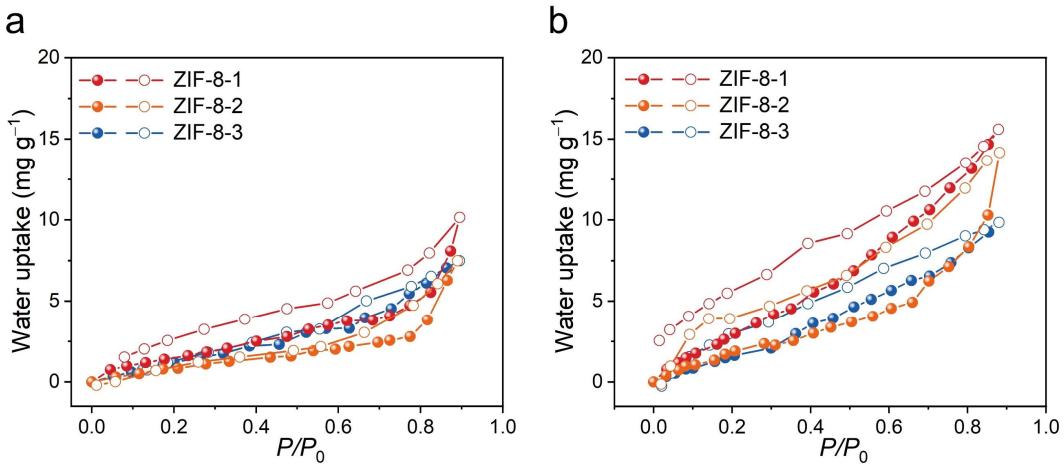


Supplementary Fig. 2. PXRD patterns and Rietveld refinement results. (a) PXRD patterns of different ZIF-8 variants. (b) PXRD Rietveld refinement results of pristine ZIF-8-1, with inset showing the relative phase composition ratios of the three crystalline phases. (c) PXRD Rietveld refinement results of pristine ZIF-8-3, with inset showing the relative phase composition ratios of the three crystalline phases.

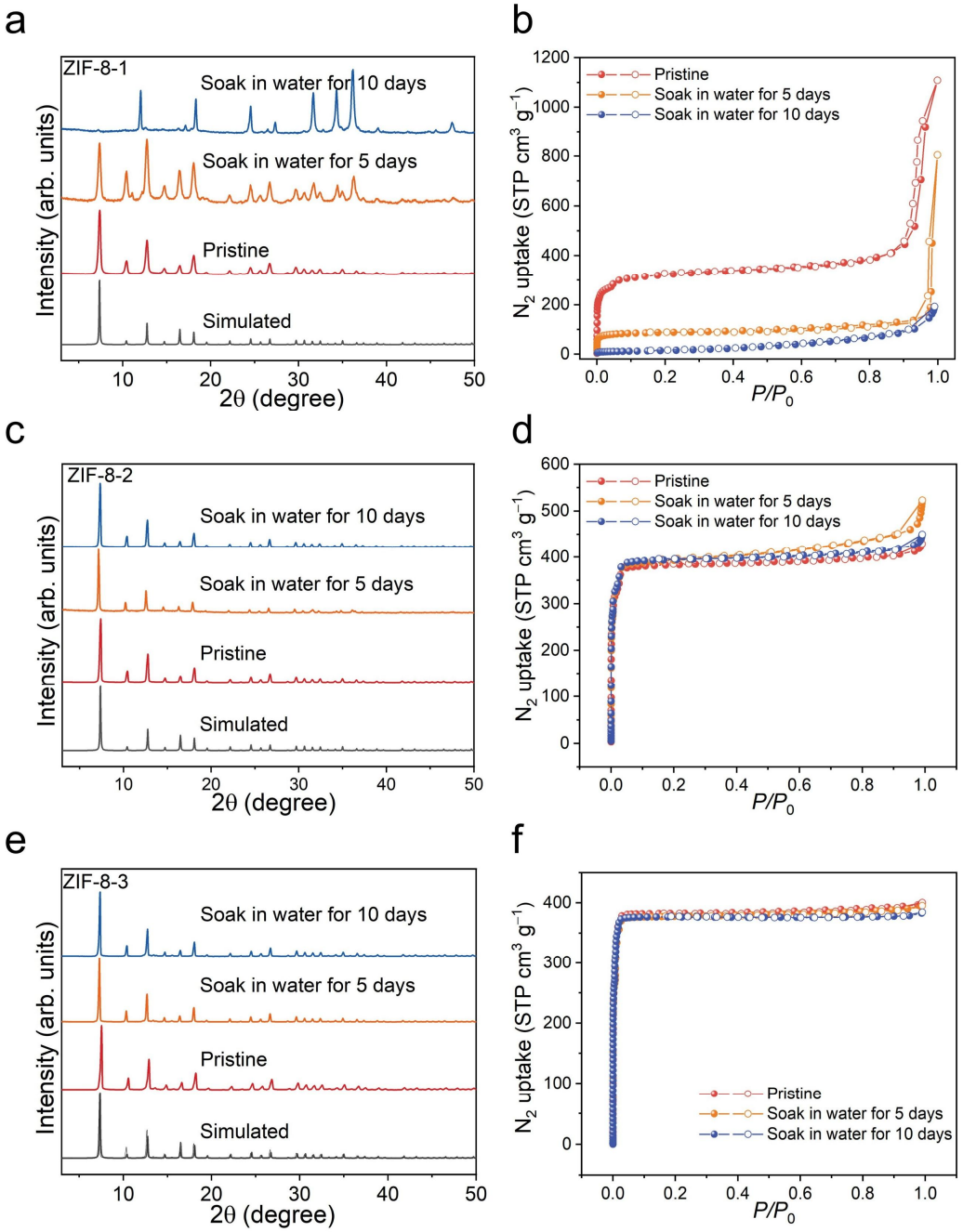


Supplementary Fig. 3. Nitrogen sorption and pore characteristics of ZIF-8 variants. (a) Nitrogen adsorption-desorption isotherms. (b) pore volume distributions. (c) pore size distributions for ZIF-8-1, ZIF-8-2, and ZIF-8-3. Inset shows pore size distributions from 0.7 to 1.8 nm.

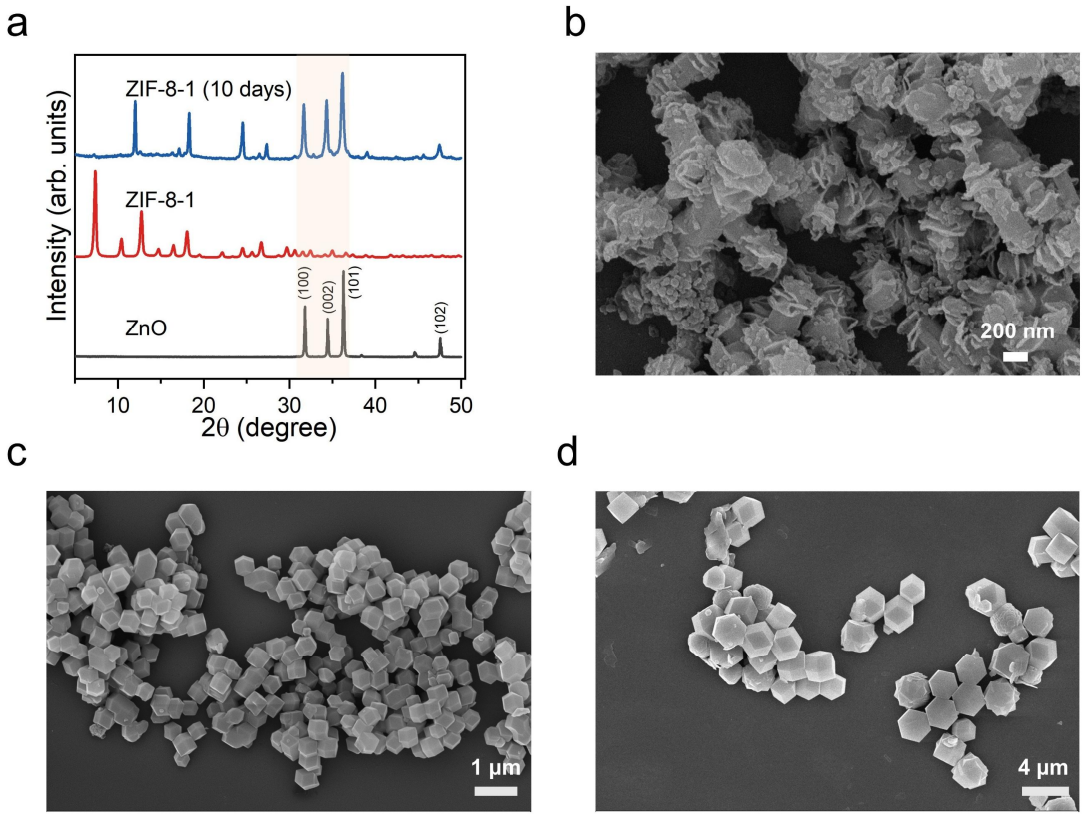
Note: For ZIF-8-1, particle aggregation caused capillary condensation to occur at high pressures, resulting in a relatively larger pore volume.



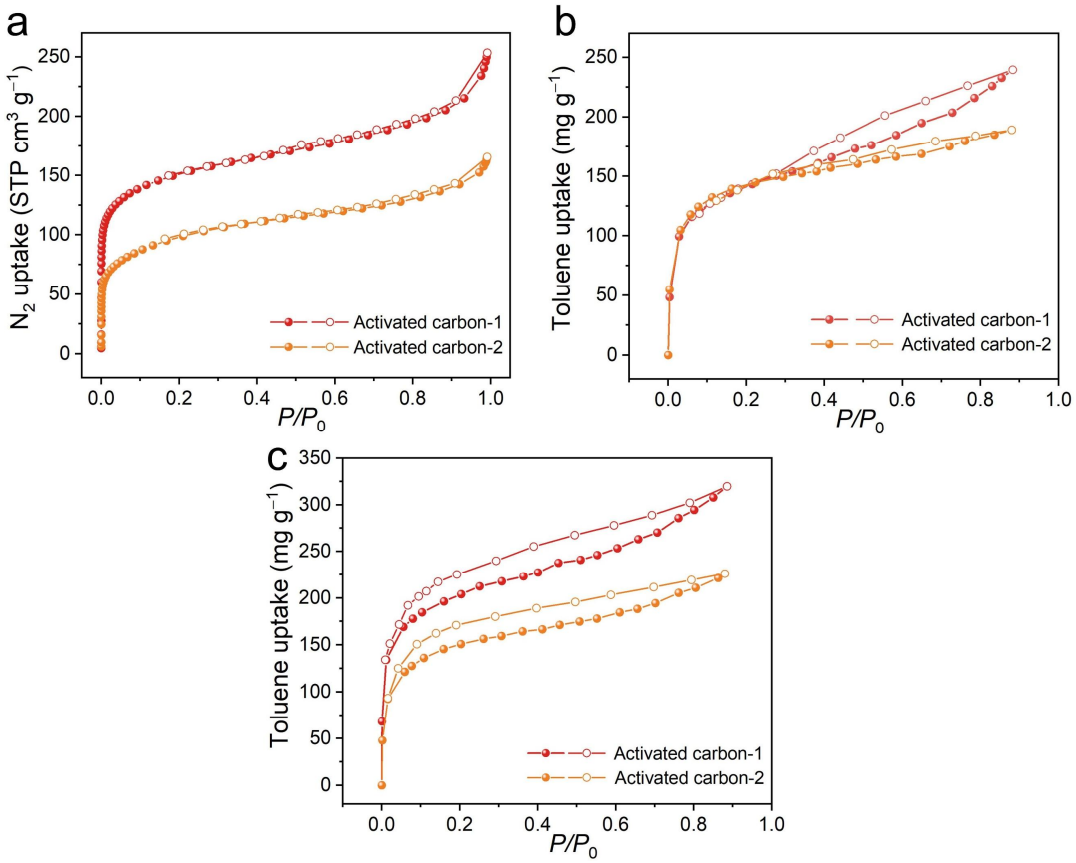
Supplementary Fig. 4. Water sorption isotherms of ZIF-8-1, ZIF-8-2, and ZIF-8-3 at (a) 25 ºC and (b) 60 ºC.



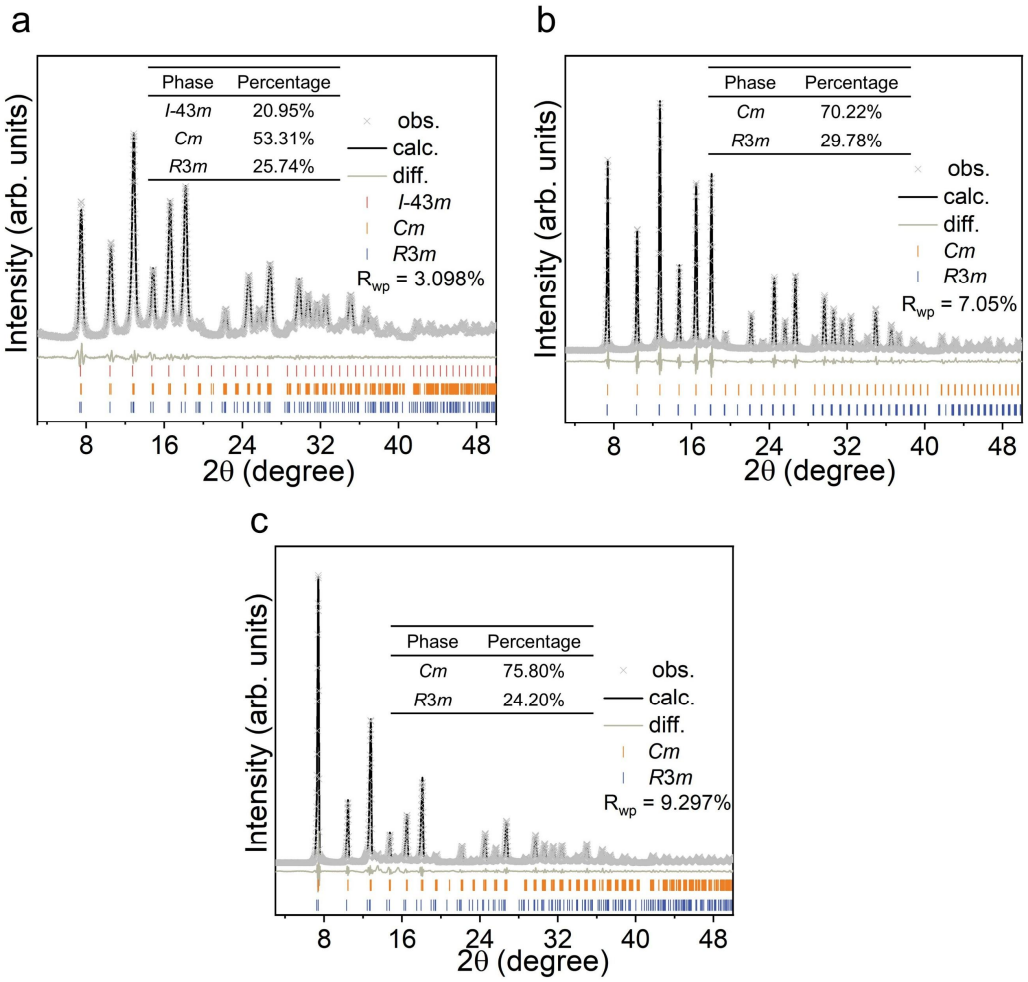
Supplementary Fig. 5. PXRD patterns and nitrogen adsorption-desorption curves after water exposure. PXRD patterns of ZIF-8-1, ZIF-8-2, and ZIF-8-3 soaked in water at 70 °C for 5 days and 10 days, shown in (a), (c), and (e), respectively. Nitrogen adsorption and desorption curves of ZIF-8-1, ZIF-8-2, and ZIF-8-3 after the same treatments are shown in (b), (d), and (f), respectively.



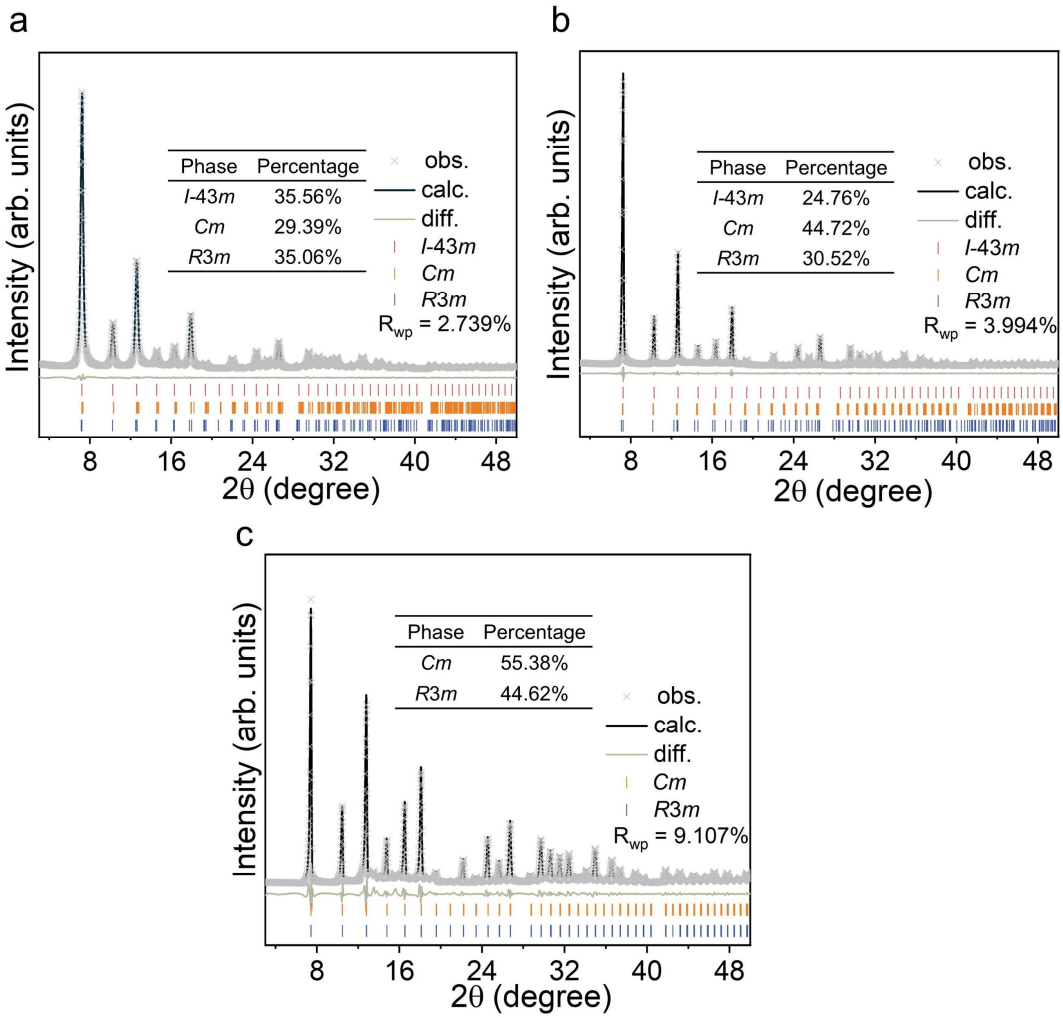
Supplementary Fig. 6. PXRD patterns and SEM images after 10 days of water immersion. (a) PXRD patterns of ZnO, pristine ZIF-8-1, and ZIF-8-1 after 10 days of water immersion. SEM images of ZIF-8-1, ZIF-8-2, and ZIF-8-3 after 10 days of water immersion are shown in (b), (c), and (d), respectively.



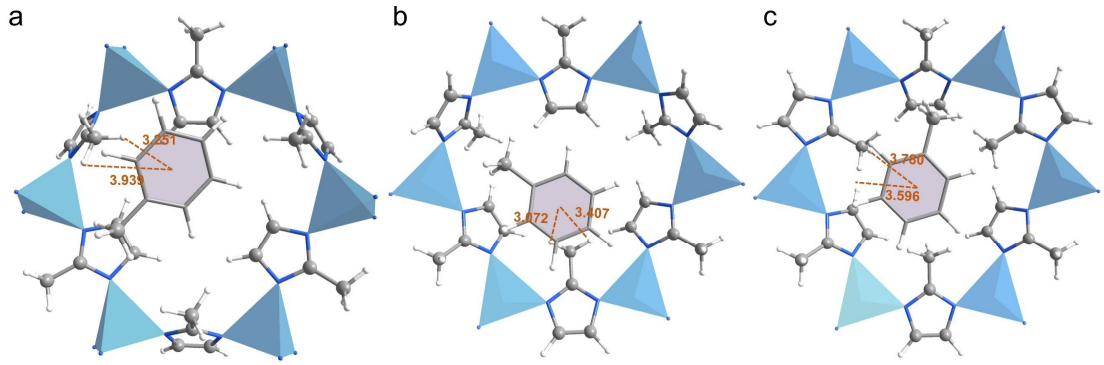
Supplementary Fig. 7. Sorption isotherms and toluene vapor sorption of activated carbons. (a) Nitrogen sorption isotherms at 77 K, (b) toluene vapor sorption curves at 298 K, and (c) toluene vapor sorption curves at 333 K of two different kinds of activated carbon.



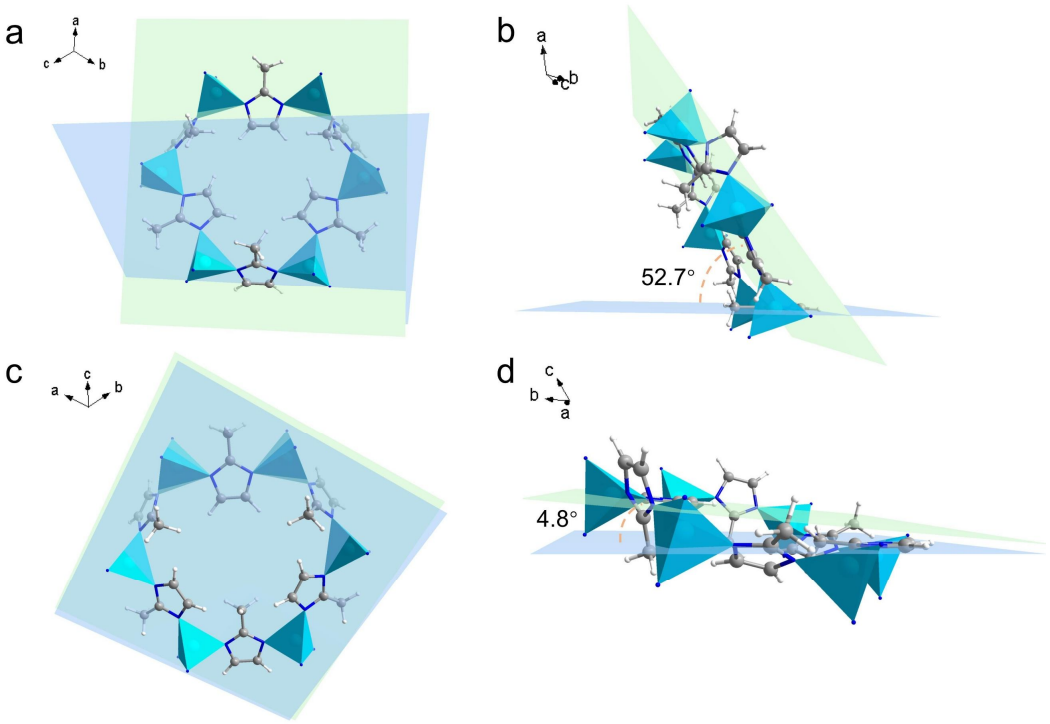
Supplementary Fig. 8. PXRD Rietveld refinement results for (a) ZIF-8-1, (b) ZIF-8-2, and (c) ZIF-8-3 after saturating adsorption with toluene. Insets show the relative phase composition ratios of the three crystalline phases.



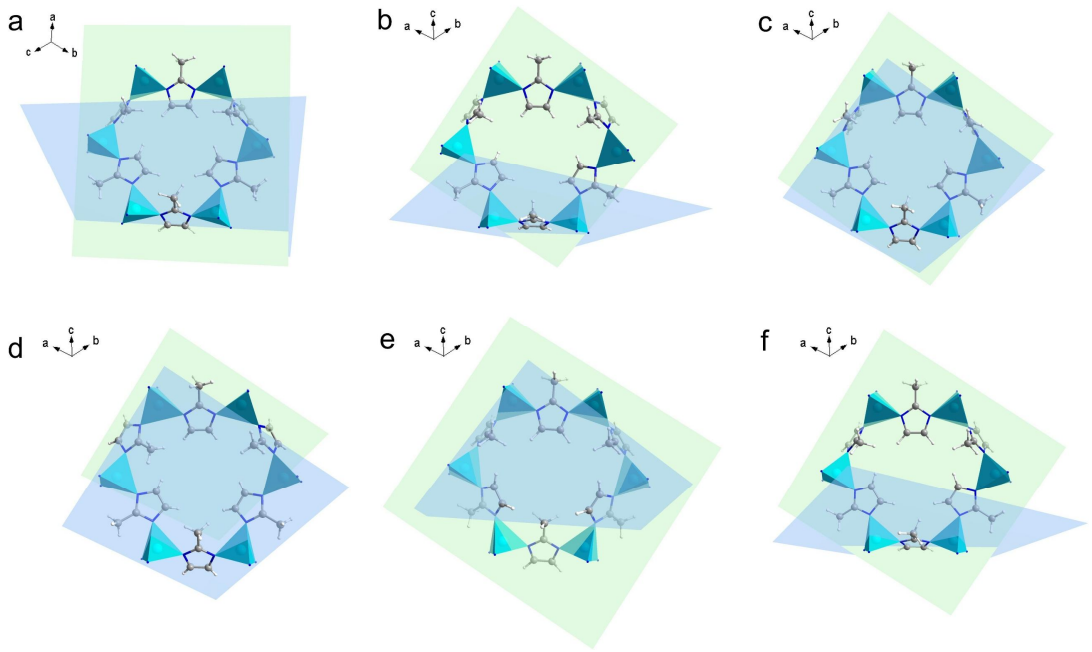
Supplementary Fig. 9. PXRD Rietveld refinement results for (a) ZIF-8-1, (b) ZIF-8-2, and (c) ZIF-8-3 after activation at 120 °C. Insets show the relative phase composition ratios of the three crystalline phases.



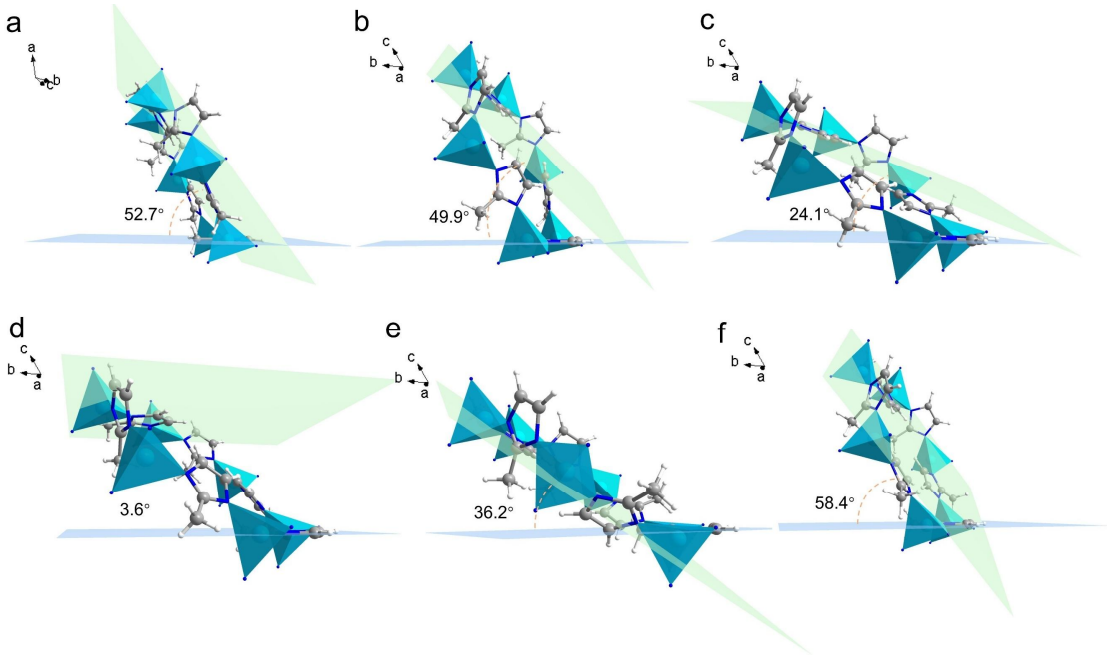
Supplementary Fig. 10. Optimal binding configurations of toluene molecules in three crystal phases (a) *I*-43*m*, (b) *Cm* and (c) *R*3*m* cavities of ZIF-8 obtained by periodic DFT calculation.



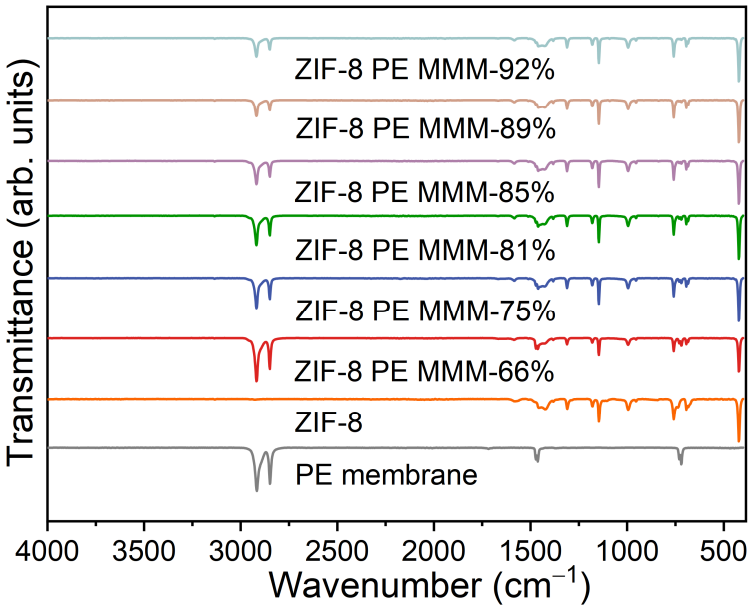
Supplementary Fig. 11. Angles between planes formed by imidazole rings at different crystal phases. Angles formed between planes constructed by two imidazole rings from opposing positions at the *I*-43*m* window, shown from different viewing angles in (a) and (b). Angles formed between planes constructed by two imidazole rings at the *Cm* window, shown from different viewing angles in (c) and (d).



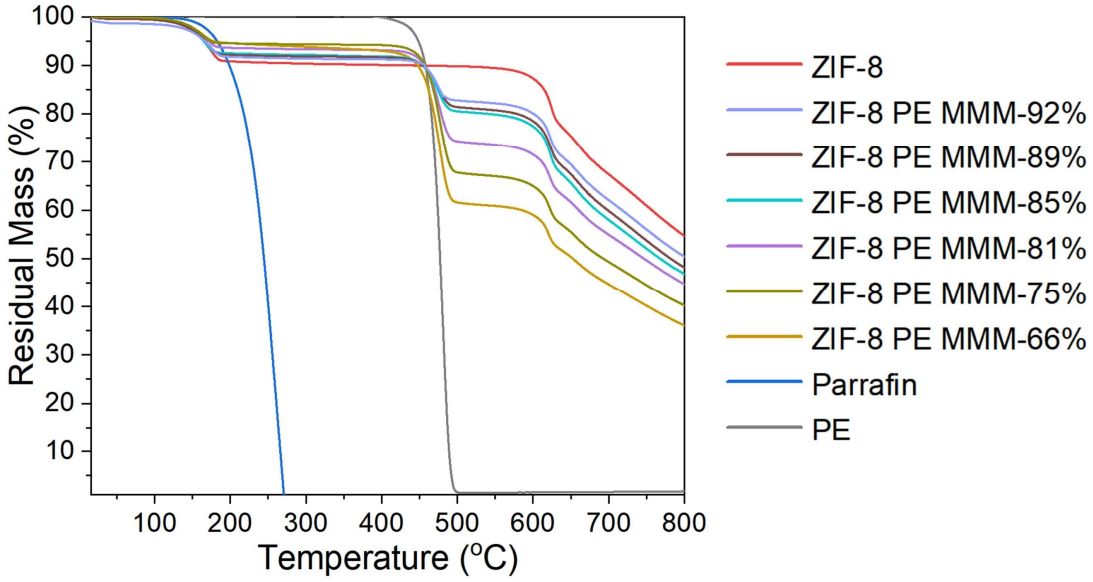
Supplementary Fig. 12. Changes in the angle between planes formed by imidazole rings during toluene adsorption and desorption in the *I*-43*m* phase. (a) Initial *I*-43*m* phase. (b) Configuration after adsorption of one toluene molecule. (c) Configuration after adsorption of four toluene molecules. (d) Configuration after adsorption of seven toluene molecules. (e) and (f) Configuration during the gradual desorption of toluene.



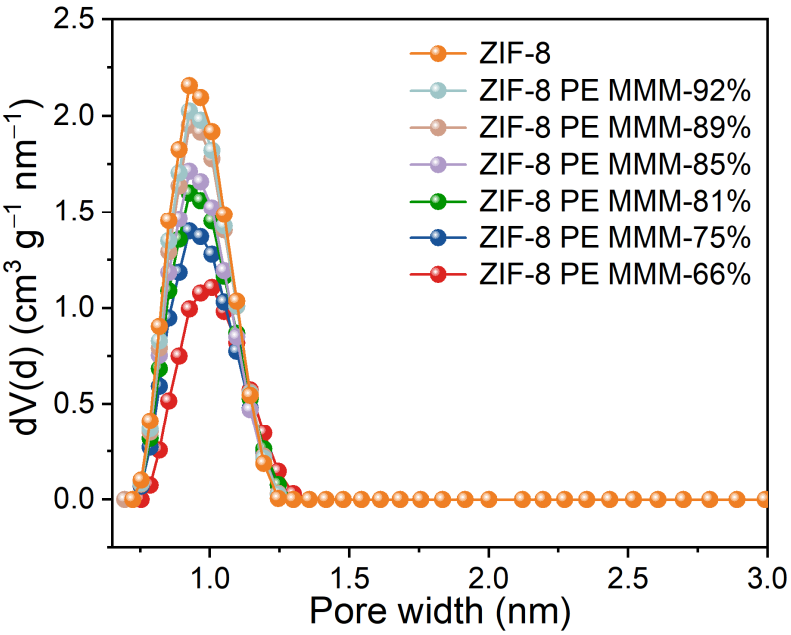
Supplementary Fig. 13. Visualization of angle changes during toluene adsorption and desorption in the *I*-43*m* phase. To better illustrate the angle variations, one of the planes formed by the 2-methylimidazole ring is shown flattened. (a) Initial *I*-43*m* phase. (b) Configuration after adsorption of one toluene molecule. (c) Configuration after adsorption of four toluene molecules. (d) Configuration after adsorption of seven toluene molecules. (e) and (f) Configuration during the gradual desorption of toluene.



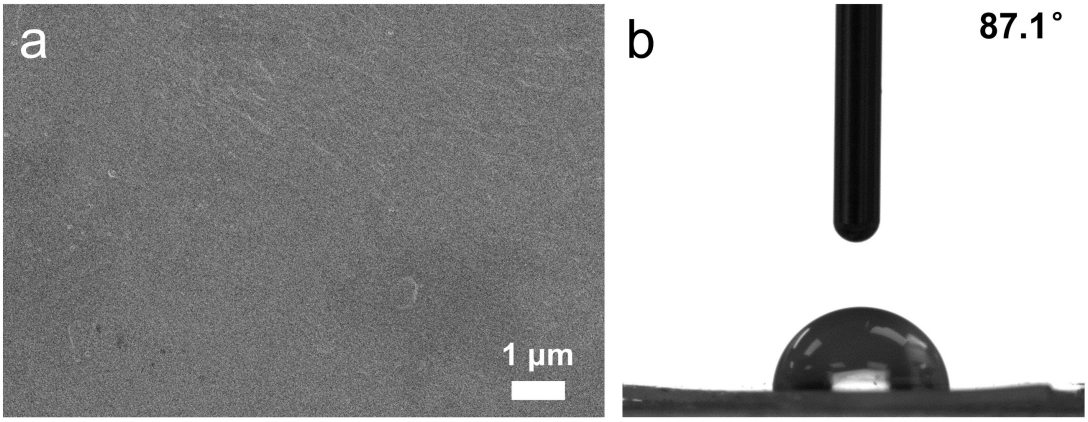
Supplementary Fig. 14. FTIR-ATR spectra of ZIF-8 PE MMMs at different loadings.



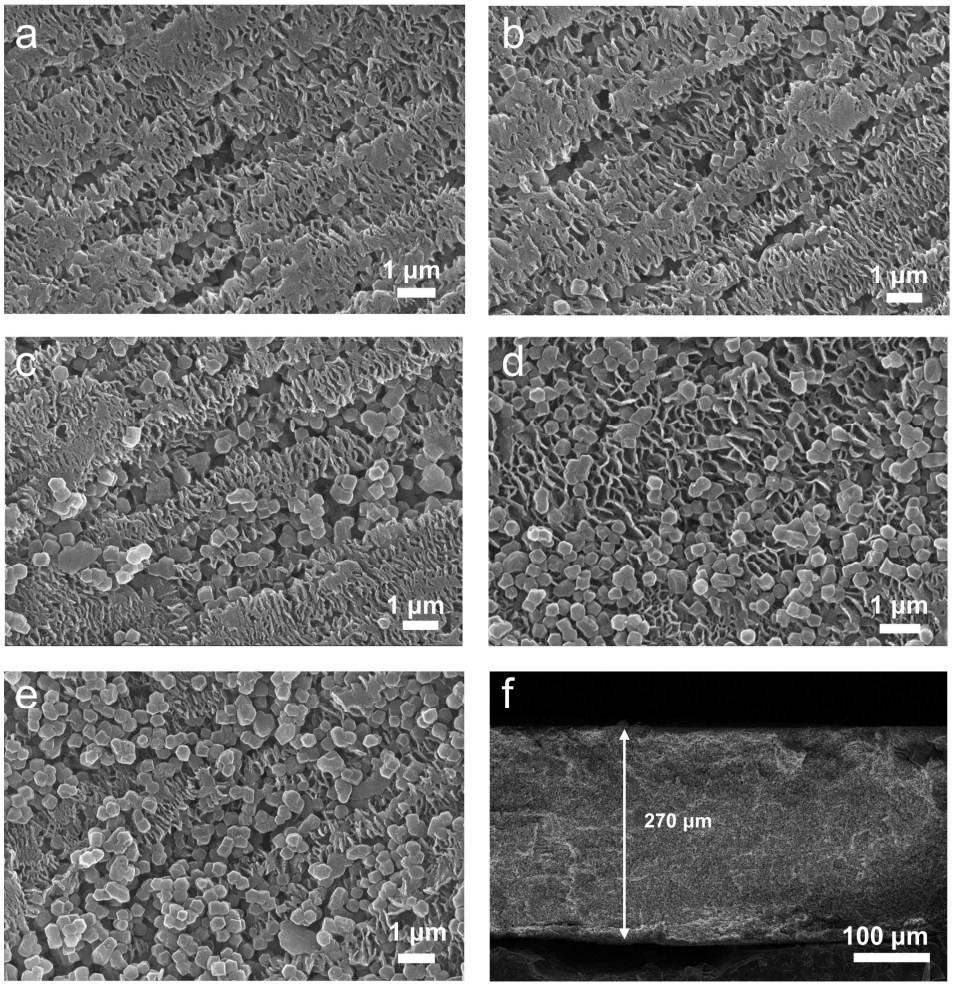
Supplementary Fig. 15. TGA curves of ZIF-8 PE MMMs with different loadings.



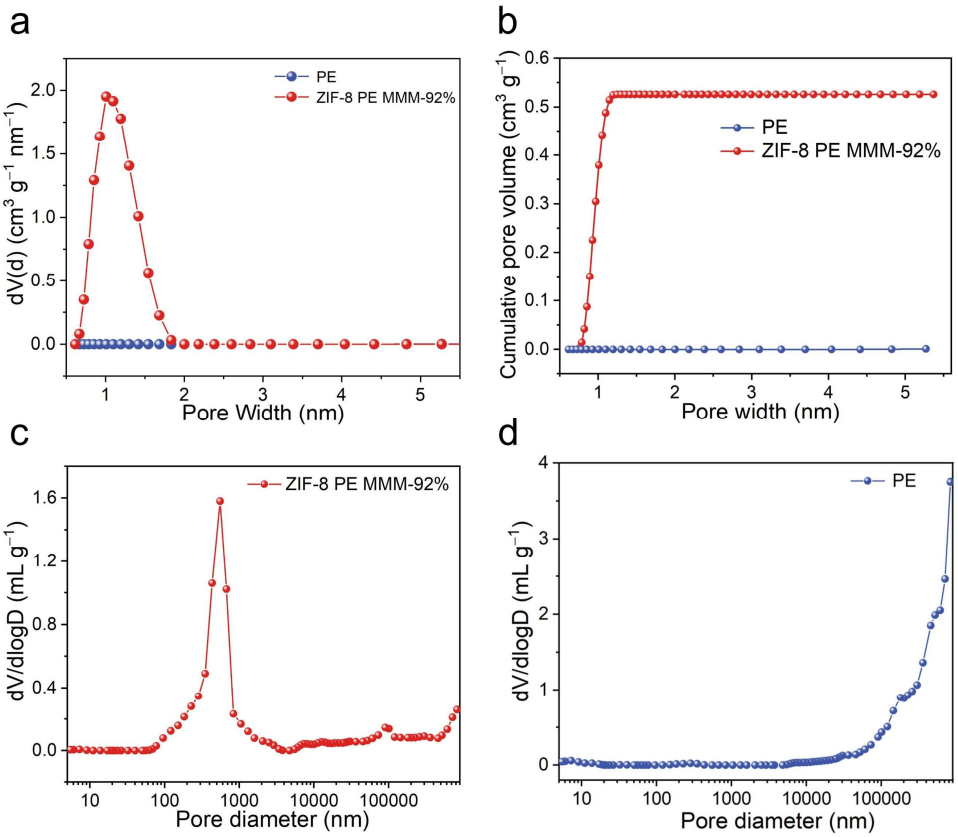
Supplementary Fig. 16. Pore size distributions of ZIF-8 PE MMMs at different loadings.



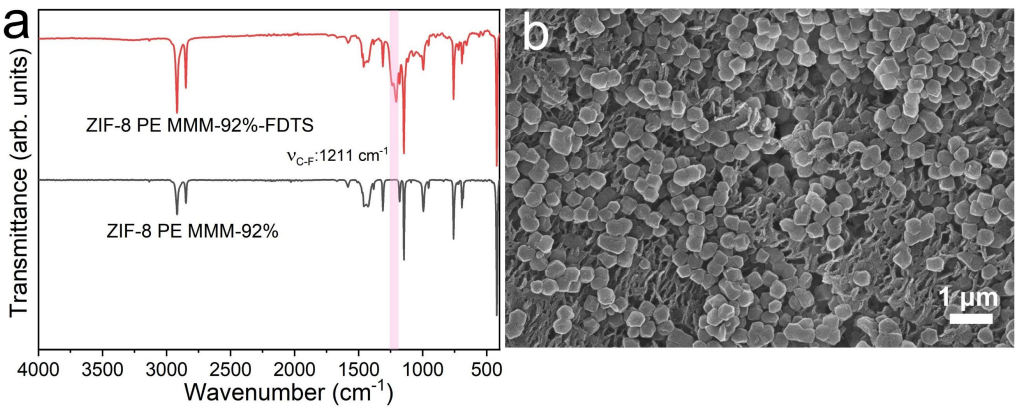
Supplementary Fig. 17. (a) SEM image and (b) water contact angle of pure PE film.



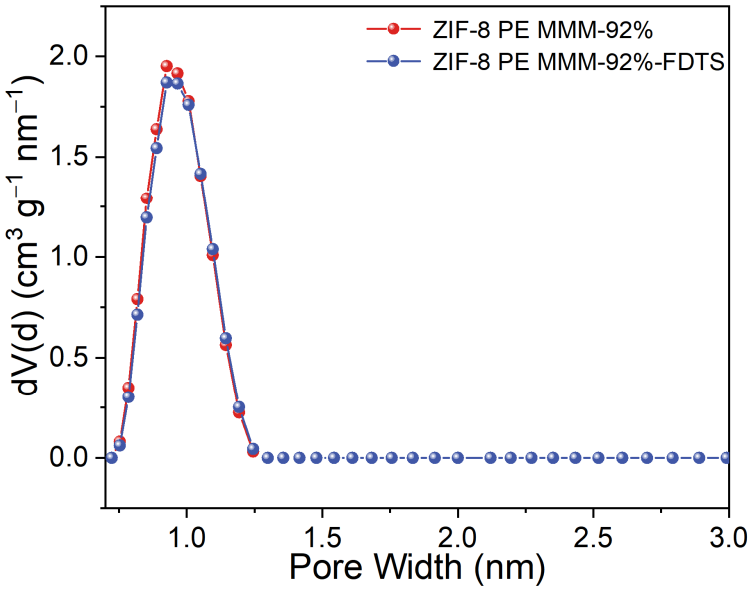
Supplementary Fig. 18. SEM images of PE MMMs with ZIF-8 loadings of (a) 66%, (b) 75%, (c) 81%, (d) 85%, and (e) 89%, and the morphology of the cross-section of (f) ZIF-8 PE MMM-92%.



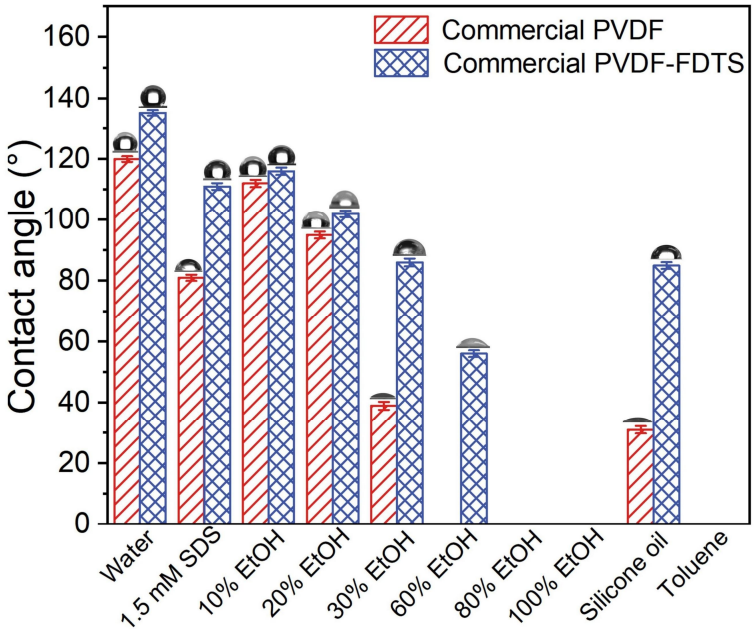
Supplementary Fig. 19. Pore structure characterization of pure PE membrane and ZIF-8 PE MMM-92%. (a) Pore size distributions of pure PE membrane and ZIF-8 PE MMM-92% from nitrogen sorption analysis. (b) Pore volume curves of pure PE membrane and ZIF-8 PE MMM-92% from nitrogen sorption analysis. (c) Mercury intrusion pore distribution curves of ZIF-8 PE MMM-92%. (d) Mercury intrusion pore distribution curves of pure PE membrane.



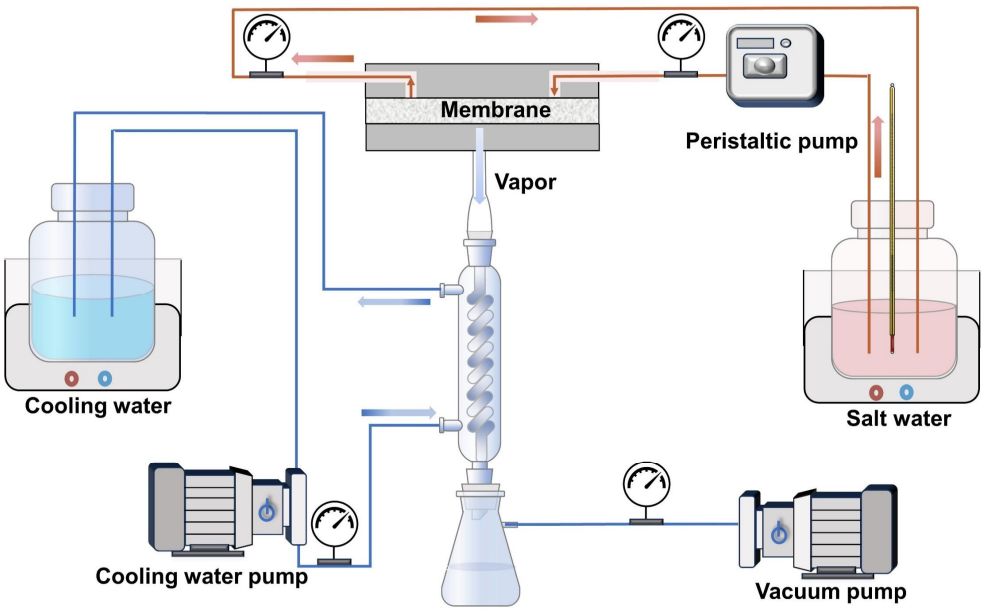
Supplementary Fig. 20. (a) FTIR-ATR spectra of ZIF-8 PE MMM-92% before and after fluorination and (b) SEM image of ZIF-8 PE MMM-92%-FDTS.



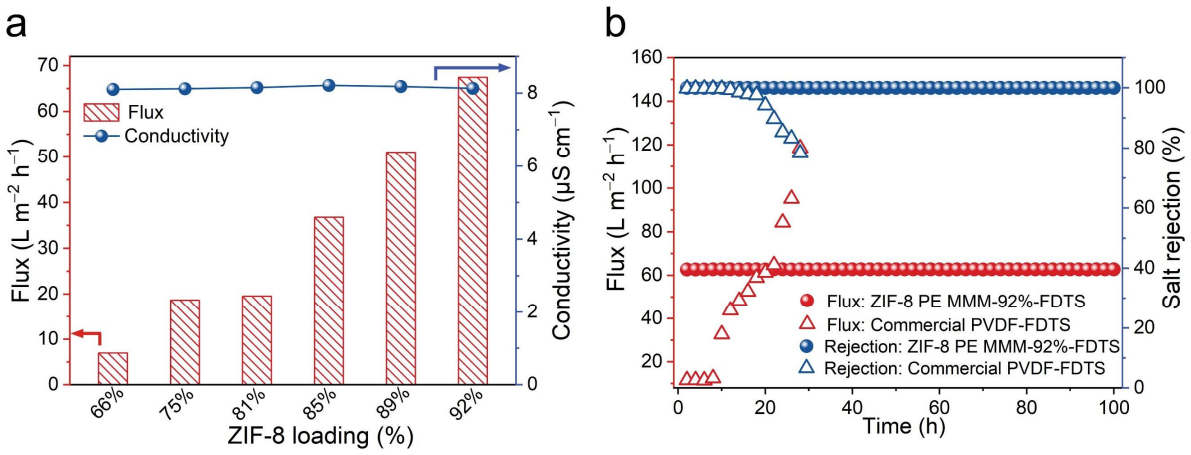
Supplementary Fig. 21. Pore size distributions of ZIF-8 PE MMM-92% before and after fluorination.



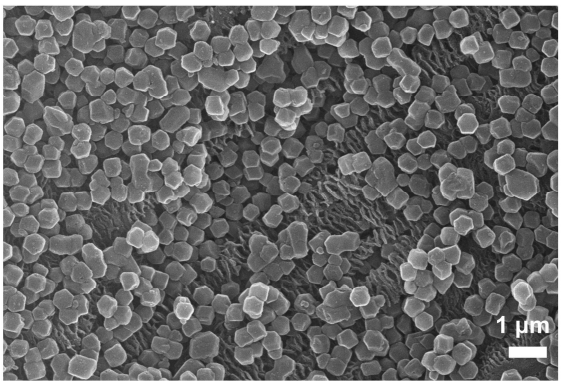
Supplementary Fig. 22. Contact angles of different liquids before and after fluorination of the commercial PVDF membrane. Error bars represent the standard deviation of three independent samples, and the centers indicate the mean values.



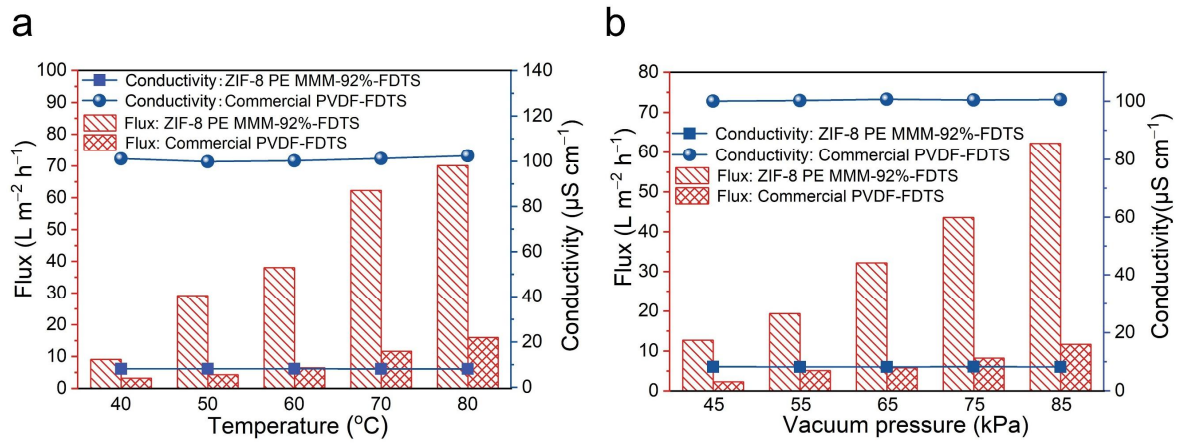
Supplementary Fig. 23. Self-made design scheme of VMD system.



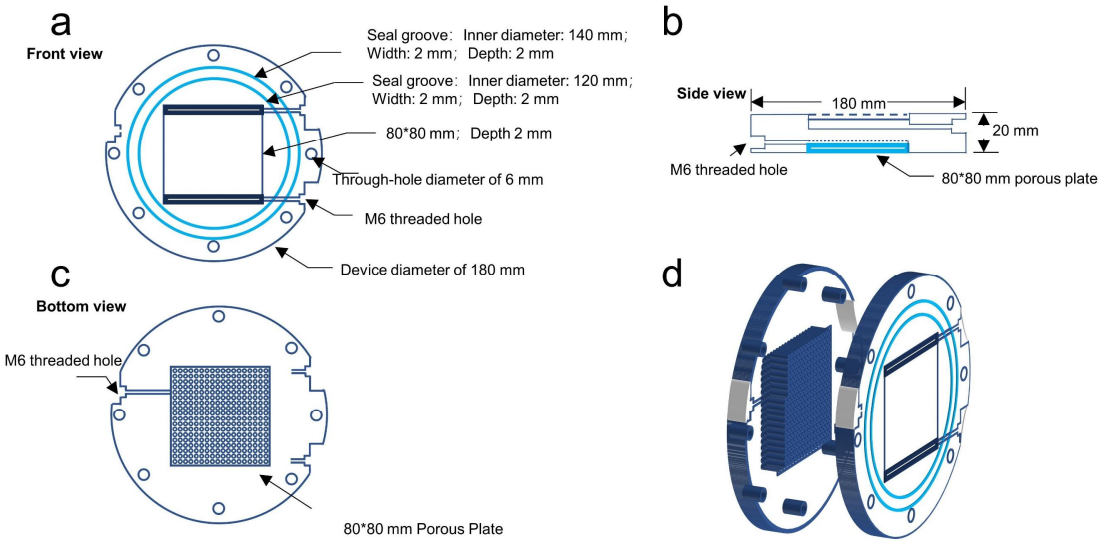
Supplementary Fig. 24. VMD performance of ZIF-8 PE MMMs and comparison with commercial membrane. (a) VMD performance of ZIF-8 PE MMMs with different loadings (feed temperature, 70 °C; salt concentration, 10.5 wt%; absolute pressure, 15 kPa). (b) VMD performance of the ZIF-8 PE MMM-92%-FDTS and commercial PVDF-FDTS membranes at 70 °C.



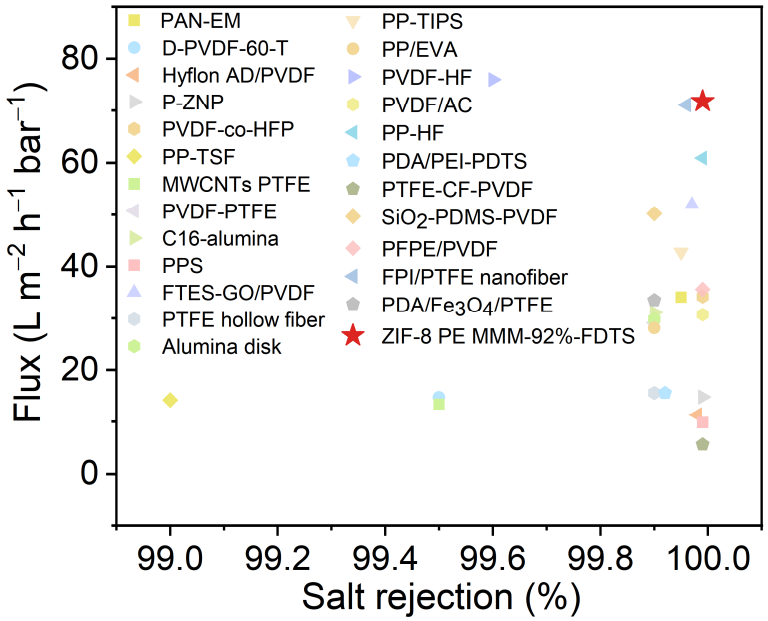
Supplementary Fig. 25. ZIF-8 PE MMM-92%-FDTS morphology after 900 hours of MD operation and a simple backwash (scale bar, 1 µm).



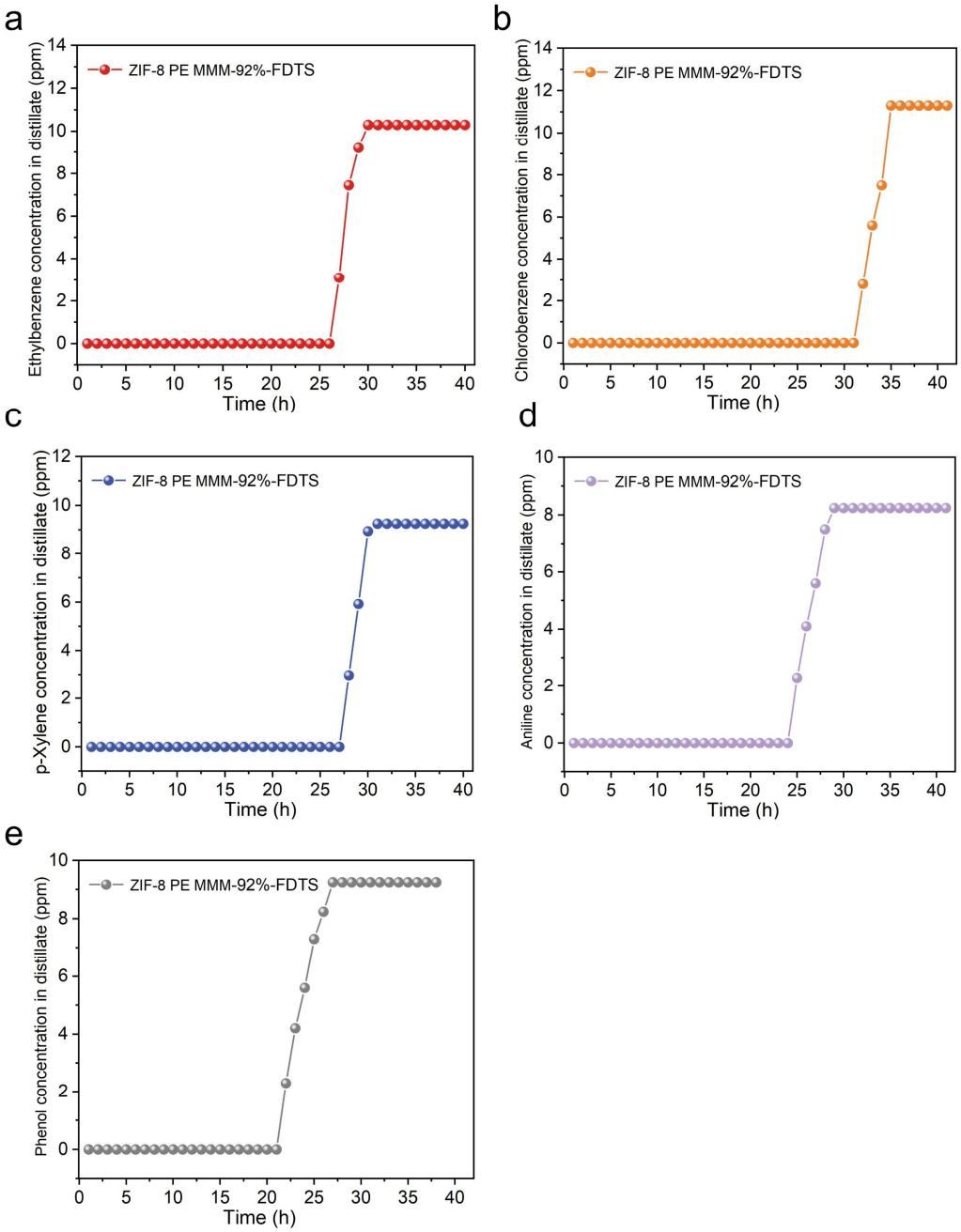
Supplementary Fig. 26. Effects of temperature and pressure on desalination performance. (a) Influence of temperature on desalination performance of ZIF-8 PE MMM-92%-FDTS and commercial PVDF-FDTS membranes. Absolute pressure and NaCl concentration were fixed at 15 kPa and 10.5 wt%. (b) Influence of absolute pressure on desalination performance of ZIF-8 PE MMM-92%-FDTS and commercial PVDF-FDTS membranes. NaCl concentration and feed temperature were fixed at 10.5 wt% and 70 °C.



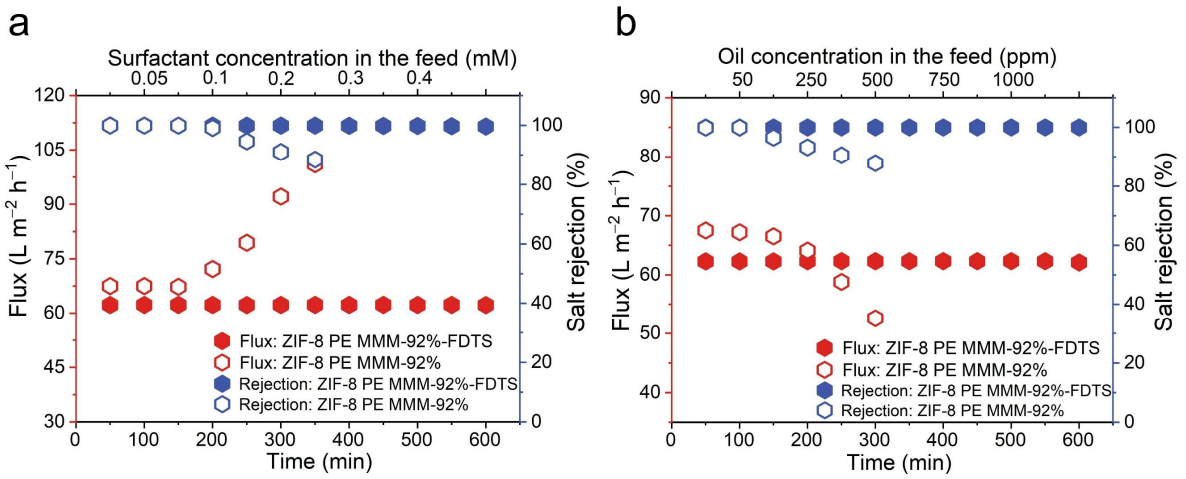
Supplementary Fig. 27. Scheme diagram of parallel stacked membrane module. (a) Front view; (b) Side view; (c) Bottom view; (d) 3D view of the membrane module.



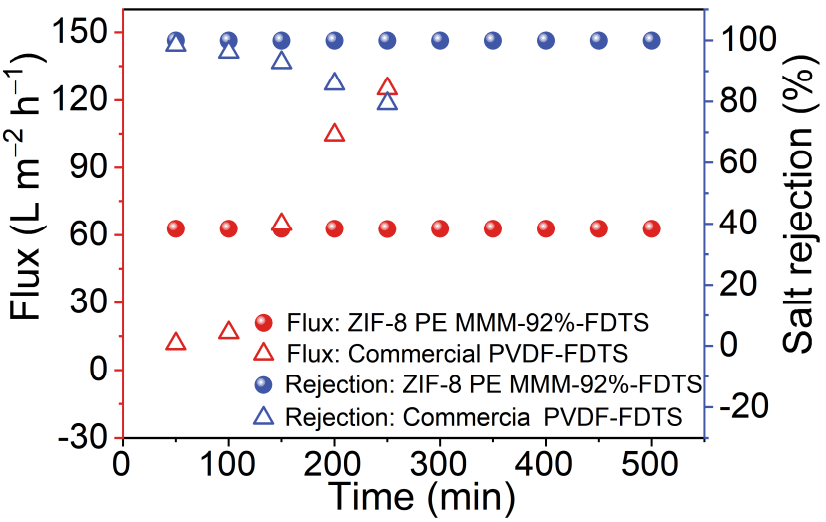
Supplementary Fig. 28. VMD performance comparison (L m^{-2} h^{-1} bar^{-1} and rejection) of our ZIF-8 PE MMM-92%-FDTS membrane versus literature reports.



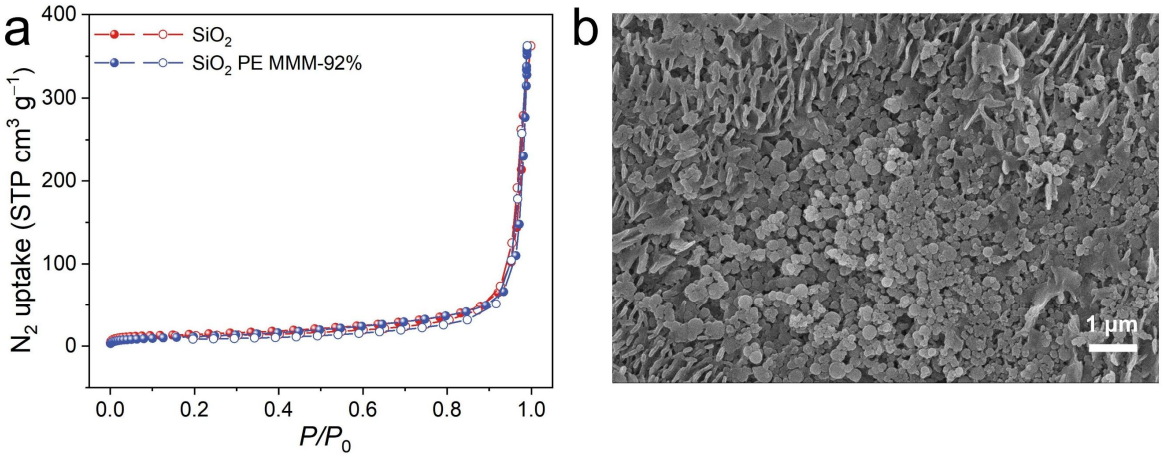
Supplementary Fig. 29. Permeate concentration profiles of various VOCs during VMD. Concentration curves over time for (a) ethylbenzene, (b) chlorobenzene, (c) p-Xylene, (d) aniline, and (e) phenol in the permeate over time using ZIF-8 PE MMM-92%-FDTS during VMD.



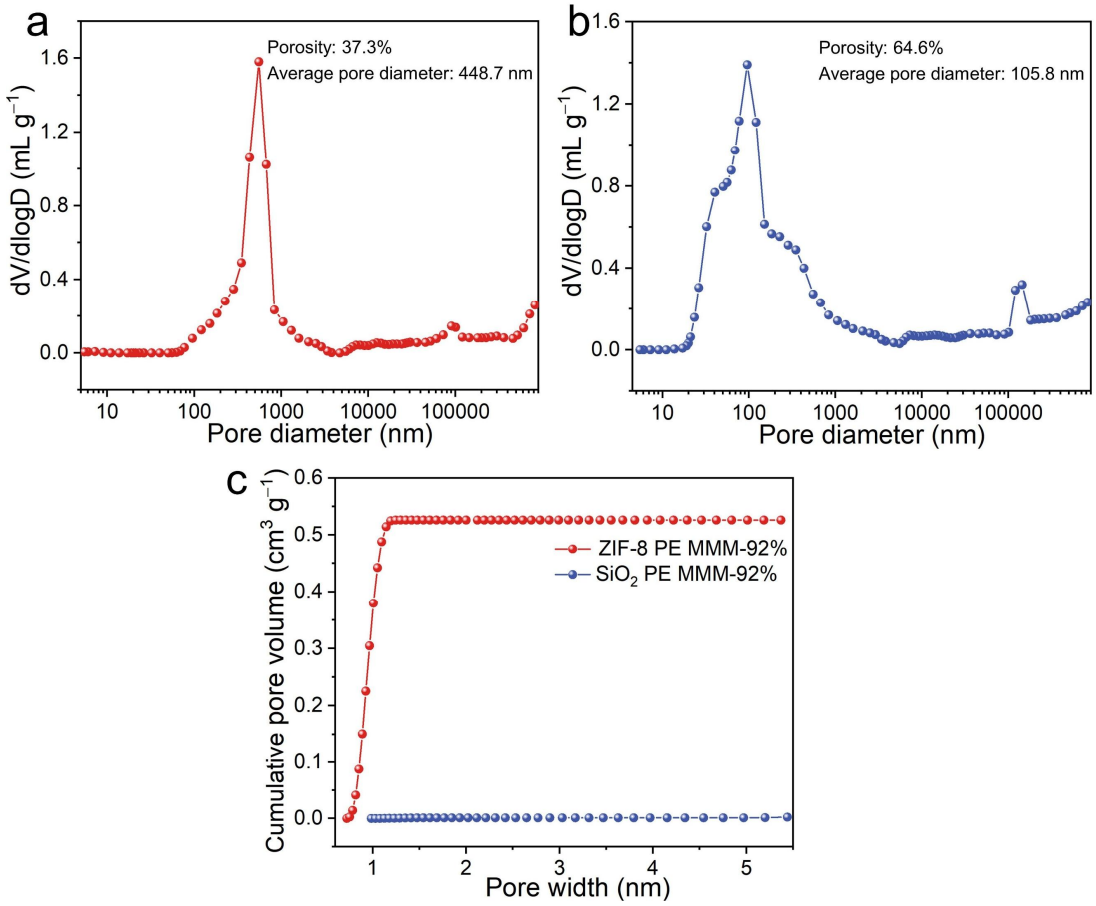
Supplementary Fig. 30. Effects of SDS and mineral oil on VMD performance. (a) Water flux and salt rejection of ZIF-8 PE MMM-92% and ZIF-8 PE MMM-92%-FDTS membranes measured in VMD. The feed solution contained 10.5 wt% NaCl, supplemented with various concentrations of SDS (0.05-0.4 mM). (b) Water flux and salt rejection of ZIF-8 PE MMM-92% and ZIF-8 PE MMM-92%-FDTS membranes measured in VMD. The feed solution contained 10.5 wt% NaCl, supplemented with various concentrations of mineral oil (50-1000 ppm).



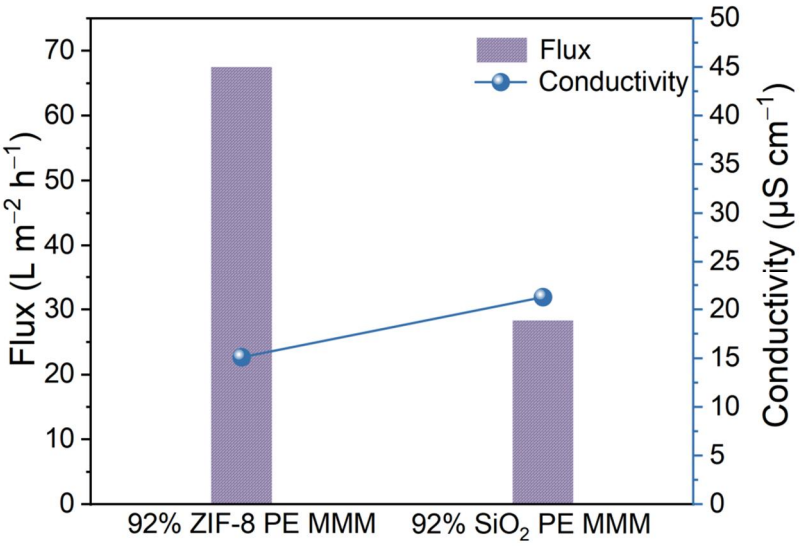
Supplementary Fig. 31. Desalination performances comparison of ZIF-8 PE MMM-92%-FDTS and commercial PVDF-FDTS membranes with brines from shale-produced water.



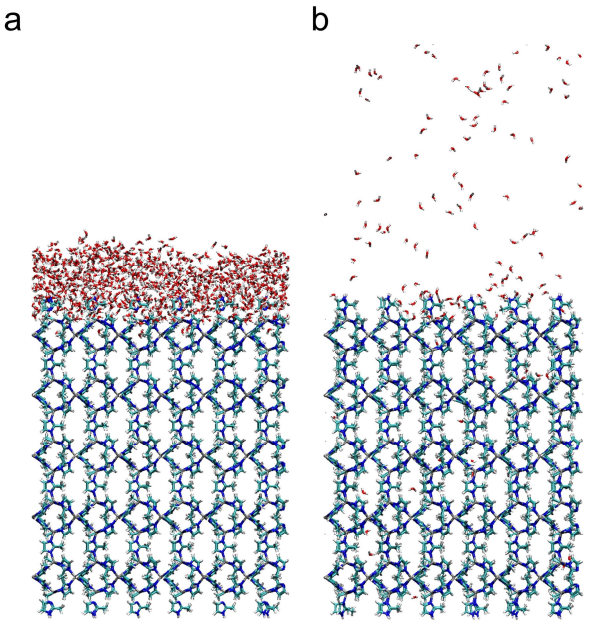
Supplementary Fig. 32. N_2 adsorption and desorption curves of (a) SiO_2 and SiO_2 PE MMM-92% and (b) SEM image of SiO_2 PE MMM-92%.



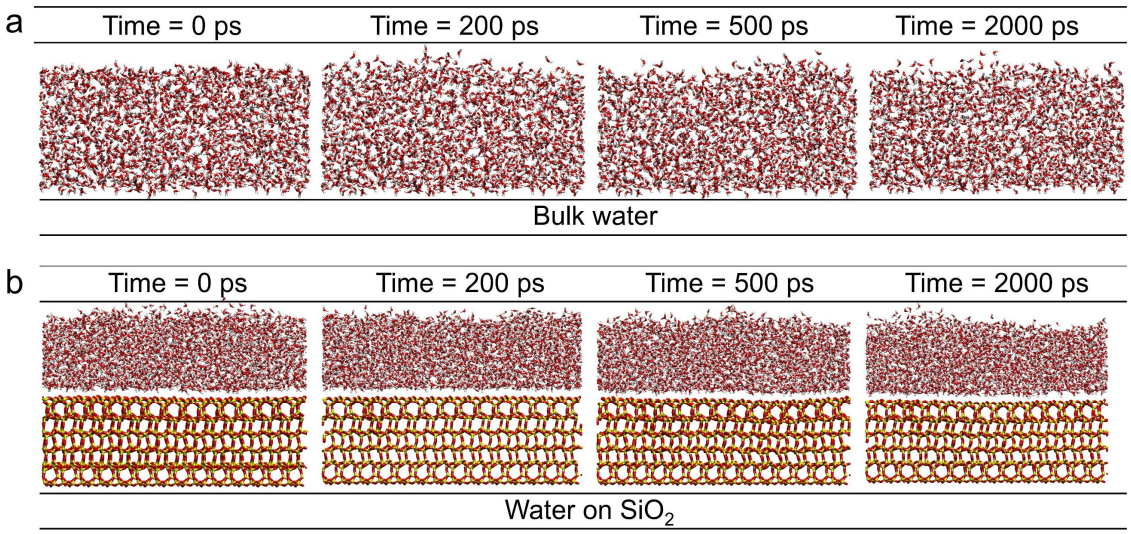
Supplementary Fig. 33. Pore structure characterization of ZIF-8 PE MMM-92% and SiO_2 PE MMM-92%. (a) and (b) Mercury intrusion pore distribution curves of ZIF-8 PE MMM-92% and SiO_2 PE MMM-92%. (c) Nitrogen sorption pore volume curves of ZIF-8 PE MMM-92% and SiO_2 PE MMM-92%.



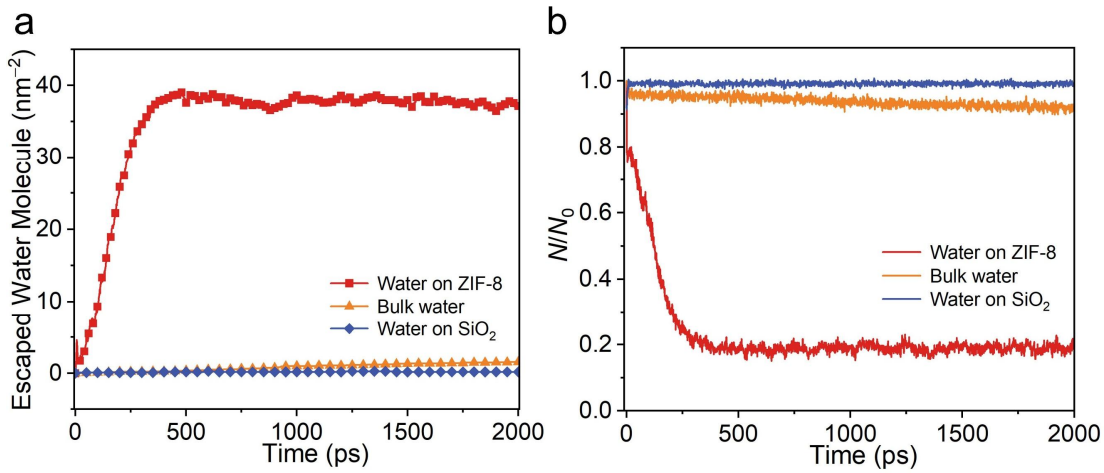
Supplementary Fig. 34. Water flux and salt rejection of SiO_2 PE MMM-92% and ZIF-8 PE MMM-92% measured in VMD with 10.5 wt% salt concentration, 70 ºC, and 85 kPa vacuum level.



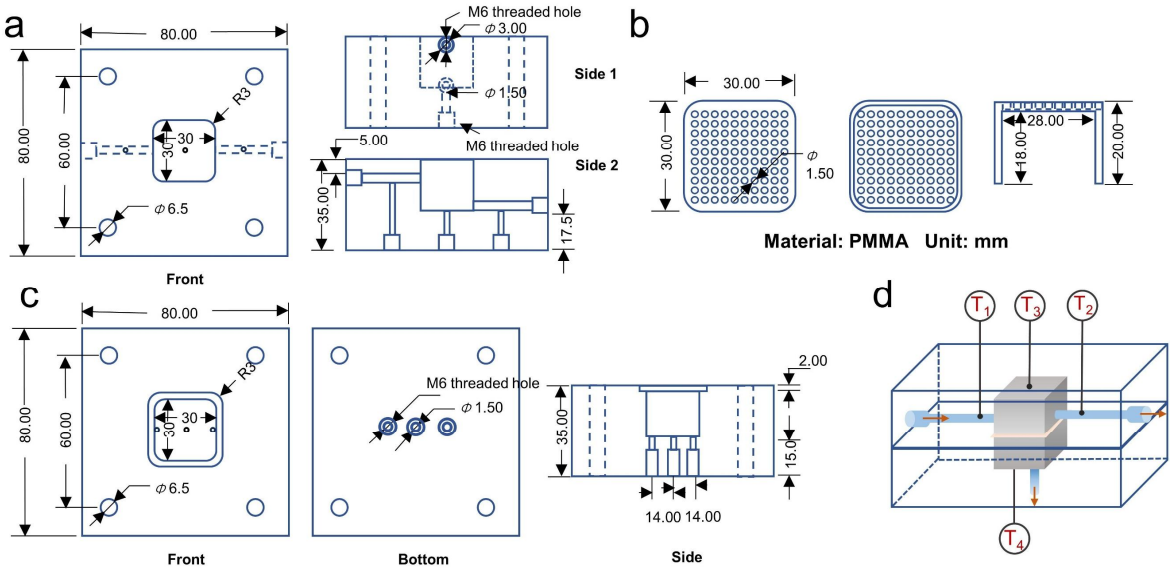
Supplementary Fig. 35. Snapshots of water evaporation on ZIF-8 at 2000 ps. (a) Snapshot of water evaporation on ZIF-8 with fixed imidazole linkages at 2000 ps. (b) Snapshot of water evaporation on ZIF-8 with freely rotating imidazole linkages at 2000 ps.



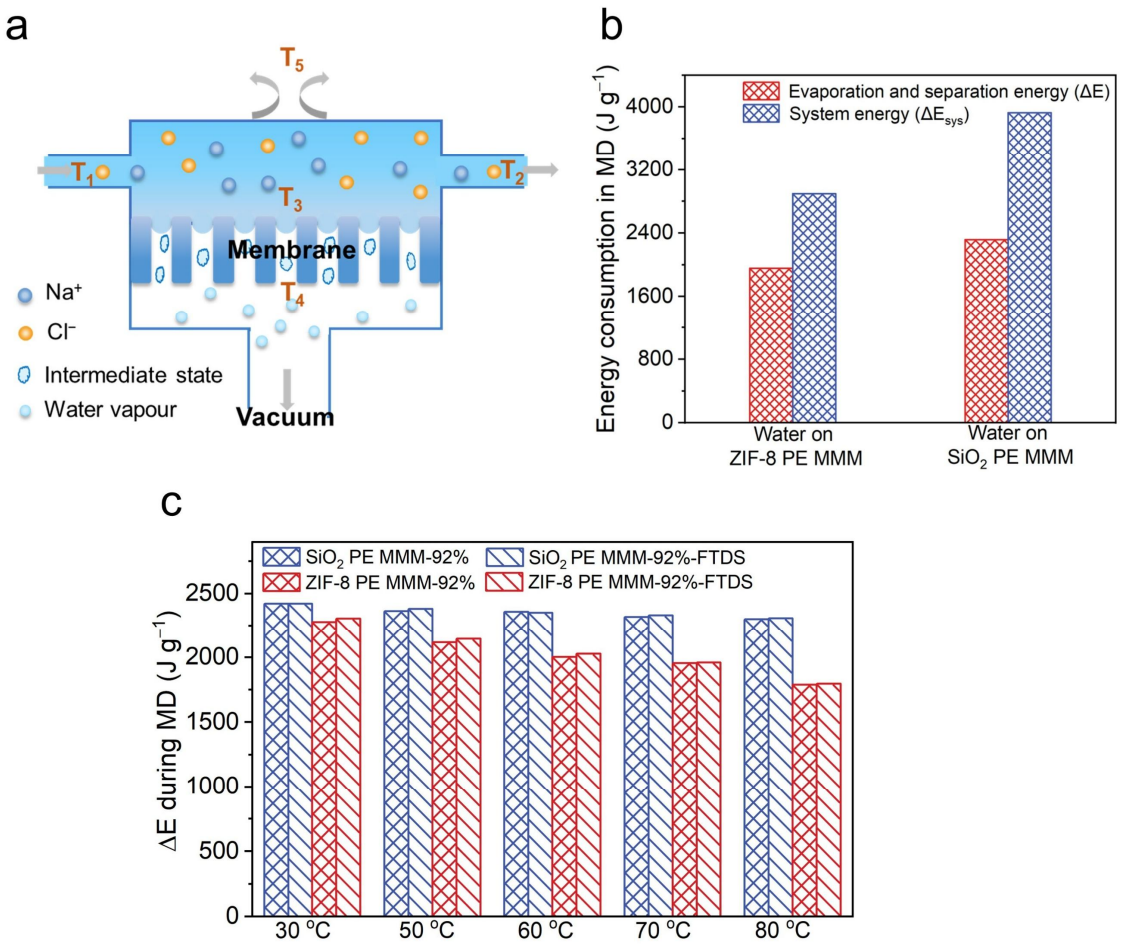
Supplementary Fig. 36. Snapshots of water evaporation from bulk and SiO_2 surface. (a) Snapshots of bulk water evaporation at 0, 200, 500 and 2000 ps. (b) Snapshots of water molecules on the SiO_2 surface during evaporation at 0, 200, 500 and 2000 ps.



Supplementary Fig. 37. Water evaporation behavior and hydrogen bond dynamics. (a) Number of water molecules escaping per square nanometer from the surfaces of ZIF-8, SiO_2 and bulk water. (b) Ratio of the number of hydrogen bonds of 0-2000 ps water molecules on the surface of ZIF-8, SiO_2 and bulk water (N) to the number of original hydrogen bonds (N_0).



Supplementary Fig. 38. Schematic diagram of membrane module setup for calculating energy in MD process. (a) Upper part of the membrane module; (b) Substrate inside the membrane module; (c) Lower part of the membrane module; (d) Complete membrane module assembly.



Supplementary Fig. 39. Energy measurement and comparison for PE MMM membranes. (a) Schematic diagram of energy measurement. (b) Comparison of evaporation and separation energy (ΔE) and total energy required to produce one unit mass of water (ΔE_{sys}) for SiO_2 PE MMM and ZIF-8 PE MMM at 70 °C. (c) Comparison of evaporation and separation energy (ΔE) for SiO_2 PE MMM and ZIF-8 PE MMM at different temperatures.

Section 3. Supplementary Tables

Supplementary Table 1. The BET surface areas of ZIF-8-1, ZIF-8-2, and ZIF-8-3 soaked in water at 70 ºC for 5 days and 10 days, respectively.

	S_{BET} m^2 g^{-1}	$S_{BET,5days}$ m^2 g^{-1}	$S_{BET,10days}$ m^2 g^{-1}
ZIF-8-1	1764	342	85
ZIF-8-2	1732	1671	1670
ZIF-8-3	1750	1729	1701

Supplementary Table 2. Concentration of Zn^{2+} in solutions after immersing ZIF-8-1, ZIF-8-2, and ZIF-8-3 in water at 70 ºC for 5 days or 10 days.

	Release of Zn^{2+} 5 days (wt%)	Release of Zn^{2+} 10 days (wt%)
ZIF-8-1	0.0074	0.0177
ZIF-8-2	0.0047	0.00577
ZIF-8-3	0.0043	0.00469

Supplementary Table 3. The elemental analysis and ICP on three ZIF-8 samples.

	N (%)	C (%)	H (%)	Zn (%)	$Radio_{N/Zn}$
ZIF-8-1	21.98	44.92	5.149	27.94	3.67
ZIF-8-2	24.00	42.66	4.582	28.75	3.90
ZIF-8-3	24.56	43.01	4.839	27.59	4.16

Supplementary Table 4. The calculation results of ZIF-8 loadings in ZIF-8 PE MMMs.

ZIF-8 loadings (wt%)	Residual mass (%)	Theoretical loadings (%)	Calculated loadings from TGA (%)
0	0	0	0
66	35.7	66	65.8
75	40.5	75	74.7
81	44.1	81	81.3
85	46.3	85	85.4
89	48.0	89	88.6
92	49.9	92	92.0
ZIF-8	54.2	100	100

Supplementary Table 5. Comparison of theoretical and actual specific surface areas of ZIF-8 PE MMMs with different loadings.

Materials	Calculated S_{BET} m^2 g^{-1}	Practical S_{BET} m^2 g^{-1}
ZIF-8 PE MMM-66%	1173	965
ZIF-8 PE MMM-75%	1333	1137
ZIF-8 PE MMM-81%	1440	1307
ZIF-8 PE MMM-85%	1511	1450
ZIF-8 PE MMM-89%	1582	1567
ZIF-8 PE MMM-92%	1636	1670
ZIF-8	1778	1778

Supplementary Table 6. Comparison of water contact angles of ZIF-8 membranes with different loadings.

Membrane materials	Contact angle θ*
PE	87°
ZIF-8	88°
ZIF-8 PE MMM-66%	118°
ZIF-8 PE MMM-75%	123°
ZIF-8 PE MMM-81%	128°
ZIF-8 PE MMM-85%	133°
ZIF-8 PE MMM-89%	138°
ZIF-8 PE MMM-92%	149°

Supplementary Table 7. Comparison of contact angles of different liquids before and after fluorination of ZIF-8 PE MMM-92%.

Liquid	ZIF-8 PE MMM-92%	ZIF-8 PE MMM-92%-FDTS
Water	149°	152°
1.5 mM SDS	115°	147°
10% EtOH	113°	146°
20% EtOH	104°	139°
30% EtOH	76°	132°
60% EtOH	62°	120°
80% EtOH	0°	112°
100% EtOH	0°	101°
Silicone oil	42°	103°
Toluene	0°	87°

Supplementary Table 8. Comparison of contact angles of different liquids before and after fluorination of commercial PVDF membrane.

Liquid	Commercial PVDF	Commercial PVDF-FDTS
Water	120°	135°
1.5 mM SDS	81°	111°
10%EtOH	112°	116°
20% EtOH	95°	102°
30% EtOH	39°	86°
60% EtOH	0	56°
80% EtOH	0	0
100% EtOH	0	0
Silicone oil	31°	85°
Toluene	0	0

Supplementary Table 9. Concentration of ZIF-8 PE MMM-92%-FDTS-immersed water after 5 days at 70 °C.

	Detection limit	ZIF-8 PE MMM-92%-FDTS-immersed water
FDTS concentration	0.20 ng L^{-1}	—

Supplementary Table 10. Comparison of the VMD performance of ZIF-8 PE MMM-92%-FDTS with membranes reported in the literature.

Membrane	Salt Conc. (wt%)	Temp. (°C)	Rejection (%)	Flux (L m^{-2} h^{-1})	Absolute Pressure (kPa)	Normalized Flux (L m^{-2} h^{-1} bar^{-1})	T (h)	Ref
PAN-EM	3.5	70	99.95	36.0	4.8	37.3	80	[8]
D-PVDF-60-T	3.5	70	99.50	14.6	2	14.7	7	[9]
Hyflon AD/PVDF	3.4	70	99.98	10.3	10	11.3	30	[10]
P-ZNP	16.7	70	99.99	12.0	20	14.8	8	[11]
PVDF-co-HFP (8%)	4.8	70	99.99	32.6	6.1	34.2	35	[12]
PP-TSF	15.0	80	99.00	13.0	10	14.2	21	[13]
MWCNTs PTFE	3.5	70	99.50	13.0	5	13.4	0.5	[14]
PVDF-PTFE	3.5	70	99.90	26.0	12	29.1	15	[15]
C16-alumina	3.0	70	99.90	30.0	5	31.1	16.7	[16]
PPS	3.5	70	99.99	8.0	20	9.8	10	[17]
FTES-GO/PVDF	3.4	50	99.97	36.4	31.3	52.0	60	[18]
PTFE hollow fiber	2.9	70	99.90	15.0	5	15.6	-	[19]
Alumina disk	3.5	70	99.90	29.3	3	29.8	2	[20]
PP-TIPS	1.0	80	99.95	41.2	5	42.8	-	[21]
PP/EVA	2.8	70	99.90	27.6	3	28.1	36	[22]
PVDF-HF	3.5	70	99.60	61.8	20	76.0	-	[23]
PVDF/AC	10.0	70	99.99	25.0	20	30.7	16	[24]
PP-HF	9.1	65	99.99	54.0	12.7	60.9	5	[25]
PDA/PEI-PDTS	3.4	70	99.92	15.0	5	15.6	50	[26]
PTFE-CF-PVDF	4.8	75	99.99	4.6	20	5.6	100	[27]
SiO_2-PDMS-PVDF	3.4	75	99.90	44.3	13	50.2	9	[28]
PFPE/PVDF	3.4	55	99.99	32.5	10	35.6	20	[29]
FPI/PTFE nanofiber membranes	3.5	70	99.96	29.4	60	71.1	120	[30]

PDA/Fe_3O_4/PTFE	7.0	65	99.90	30.6	10	33.5	10	[31]
Commercial Immobilon-P^{SQ} PVDF	16.7	70	-	16.0	20	19.7	-	[11]
VALQUA PTFE	7	65	-	30.6	10	33.5	10	[31]
Commercial PVDF	10.5	70	99.80	23.0	15	26.6	-	This work
PVDF-FDTS	10.5	70	99.82	12.0	15	13.9	10	This work
ZIF-8 PE MMM-92%-FDTS	10.5	70	99.99	62.0	15	71.8	300	This work

Note: The reported BPPF6@PVDF[32] and carbon composite membranes[33] were not included in the table due to the much lower absolute pressure (1 kPa) used for MD testing. Additionally, considering potential large-scale production, we did not include our previously reported pure covalent organic framework membrane[34].

Supplementary Table 11. Concentration of benzene series in the distillation after MD process using ZIF-8 PE MMM-92%-FDTS and PVDF-FDTS.

Benzene series	Guideline values[a] / ppm	Concentration of benzene in distillate / ppm	
		ZIF-8 PE MMM-92%-FDTS	PVDF-FDTS
Toluene	0.7	0	241
Ethylbenzene	0.3	0	254
Chlorobenzene	0.3	0	268
p-Xylene	0.5	0	276
Aniline	0.001	0	216
Phenol	0.002	0	201

a. Background document for preparation of WHO Guidelines for drinking-water quality. Geneva, World Health Organization.

Supplementary Table 12. ZIF-8 PE MMM-92%-FDTS membrane is capable of treating shale gas wastewater containing approximately 10 ppm benzene per unit area, as estimated from performance data at 200 ppm.

	Penetration time / h	Wastewater treatment capacity / mL cm^{-2}
Toluene	600	3720
Ethylbenzene	520	3220
Chlorobenzene	620	3840
p-Xylene	540	3340
Aniline	500	3100
Phenol	440	2720

Supplementary Table 13. The total porosity of ZIF-8 PE MMM-92% and SiO_2 PE MMM-92%.

	Porosity (0- 5.5 nm)	Porosity (5.5 nm- 825 μm)	Total porosity
ZIF-8 PE MMM-92%	26.1%	37.3%	63.4%
SiO_2 PE MMM-92%	0.12%	64.6%	64.7%

Supplementary Table 14. Calculation of thermal conductivities in ZIF-8 PE MMM-92%.

T (°C)	30	50	60	70	80
Thermal diffusivity ($\times 10^{-6}$ m^2 s^{-1})	0.172	0.164	0.155	0.151	0.142
Specific heat capacity (J kg^{-1} K^{-1})	1697	1708	1739	1771	1804
Density (kg m^{-3})			495.9		
Thermal conductivity (W m^{-1} K^{-1})	0.1447	0.1389	0.1337	0.1326	0.1270

Thermal conductivity (h_m) = Thermal diffusivity × Specific heat capacity × Density

Supplementary Table 15. Energy calculation of ZIF-8 PE MMM-92%.

T_1 (°C)	T_2 (°C)	T_3 (°C)	T_4 (°C)	T_5 (°C)	λ_{PMMA}[35] (W m^{-1} K^{-1})	J (L m^{-2} h^{-1})	ΔE (J g^{-1})
31.24	30.82	32.14	23.93	23.29	0.1917	9.54	2276.06
50.62	49.32	51.94	25.45	24.28	0.1944	31.20	2116.97
60.06	58.37	60.83	25.12	24.70	0.1958	42.50	2001.88
70.03	67.55	70.66	27.90	24.99	0.1971	68.17	1955.40
80.01	77.47	81.25	31.07	24.72	0.1984	73.12	1787.93

Supplementary Table 16. The calculation of thermal conductivities in SiO_2 PE MMM-92%.

T (^oC)	30	50	60	70	80
Thermal diffusivity ($\times 10^{-6}$ m^2 s^{-1})	0.164	0.159	0.158	0.158	0.156
Specific heat capacity (J kg^{-1} K^{-1})	1564	1605	1614	1615	1635
Density (kg m^{-3})			478.2		
Thermal conductivity (W m^{-1} K^{-1})	0.1226	0.1220	0.1219	0.1220	0.1220

Thermal conductivity (h_m) = Thermal diffusivity × Specific heat capacity × Density

Supplementary Table 17. The energy calculation of SiO_2 PE MMM-92%.

T_1 (°C)	T_2 (°C)	T_3 (°C)	T_4 (°C)	T_5 (°C)	λ_{PMMA} (W m^{-1} K^{-1})	J (L m^{-2} h^{-1})	ΔE (J g^{-1})
31.15	30.98	31.38	27.27	24.01	0.1917	3.43	2420.28
50.02	49.34	50.13	26.43	23.97	0.1944	11.50	2361.45
60.17	59.07	61.61	26.74	23.89	0.1958	19.90	2357.96
70.02	68.57	71.37	31.53	24.79	0.1971	28.70	2316.55
80.02	78.33	80.98	31.79	24.58	0.1984	32.50	2300.28

Supplementary Table 18. Energy calculation of ZIF-8 PE MMM-92%-FDTS.

T_1 (°C)	T_2 (°C)	T_3 (°C)	T_4 (°C)	T_5 (°C)	λ_{PMMA} (W m^{-1} K^{-1})	J (L m^{-2} h^{-1})	ΔE (J g^{-1})
30.07	29.68	30.85	22.62	22.73	0.1917	8.50	2303.52
50.08	48.81	50.98	21.17	22.68	0.1944	28.30	2142.73
60.07	58.37	61.24	23.52	22.55	0.1958	41.30	2027.47
70.08	67.73	70.87	25.85	23.15	0.1971	62.17	1960.03
80.09	77.56	80.82	26.24	23.64	0.1984	70.12	1795.49

Supplementary Table 19. The energy calculation of SiO_2 PE MMM-92%-FDTS.

T_1 (°C)	T_2 (°C)	T_3 (°C)	T_4 (°C)	T_5 (°C)	λ_{PMMA} (W m^{-1} K^{-1})	J (L m^{-2} h^{-1})	ΔE (J g^{-1})
30.06	29.97	30.73	27.35	24.01	0.1917	1.32	2421.02
50.00	49.42	50.73	27.83	23.62	0.1944	8.66	2381.26
60.02	59.18	60.61	26.67	23.71	0.1958	12.42	2350.49
70.05	68.92	71.13	30.99	23.11	0.1971	18.64	2329.38
80.01	78.67	80.63	31.21	23.22	0.1984	21.60	2306.53

Section 4. Supplementary References

1. Van Der Spoel, D. et al. GROMACS: fast, flexible, and free. *J. Comput. Chem.* **26**, 1701–1718 (2005).
2. Li, L. et al. Molecular-level understanding of surface roughness boosting segregation behavior at the ZIF-8/ionic liquid interfaces. *Langmuir* **38**, 4175–4187 (2022).
3. Berendsen, H. J. C., Grigera, J. R. & Straatsma, T. P. The missing term in effective pair potentials. *J. Phys. Chem.* **91**, 6269–6271 (1987).
4. Emami, F. S. et al. Force field and a surface model database for silica to simulate interfacial properties in atomic resolution. *Chem. Mater.* **26**, 2647–2658 (2014).
5. Humphrey, W., Dalke, A. & Schulten, K. VMD: visual molecular dynamics. *J. Mol. Graphics* **14**, 33–38 (1996).
6. Plimpton, S. Fast parallel algorithms for short-range molecular dynamics. *J. Comput. Phys.* **117**, 1–19 (1995).
7. Liu, Z., Liu, Z. & Liu, R. Fast evaporation of ultra-thin pure and saline water film through functionalized holey graphene membrane. *Int. Commun. Heat Mass Transfer* **140**, 106542 (2023).
8. Liu, L. et al. A novel plasma-induced surface hydrophobization strategy for membrane distillation: etching, dipping and grafting. *J. Membr. Sci.* **499**, 544–554 (2016).
9. Lu, K., Zuo, J., Chang, J., Kuan, H. & Chung, T. Omniphobic hollow-fiber membranes for vacuum membrane distillation. *Environ. Sci. Technol.* **52**, 4472–4480 (2018).
10. Zhang, Y. et al. Enhancing wetting resistance of poly(vinylidene fluoride) membranes for vacuum membrane distillation. *Desalination* **415**, 58–66 (2017).
11. Wang, M. et al. ZnO nanorod array modified PVDF membrane with superhydrophobic surface for vacuum membrane distillation application. *ACS Appl. Mater. Interfaces* **10**, 13452–13461 (2018).
12. Shah, A. A. et al. Origin of fluoropolymer affinity toward water and its impact on membrane performance. *ACS Appl. Polym. Mater.* **2**, 5249–5258 (2020).
13. Zhang, L. et al. Construction of PP membranes with robust interfacial stability by ALD and fluorinated grafting for high salt solution distillation. *Desalination* **548**, 116291 (2023).
14. Huang, Q., Liu, H., Wang, Y. & Xiao, C. A hybrid electric field assisted vacuum membrane distillation method to mitigate membrane fouling. *RSC Adv.* **8**, 18084–18092 (2018).
15. Dong, Z., Ma, X., Xu, Z., You, W. & Li, F. Superhydrophobic PVDF–PTFE electrospun nanofibrous membranes for desalination by vacuum membrane distillation. *Desalination* **347**, 175–183 (2014).
16. Chen, X. et al. Tubular hydrophobic ceramic membrane with asymmetric structure for water desalination via vacuum membrane distillation process. *Desalination* **443**, 212–220 (2018).
17. Fan, T., Li, Z., Cheng, B. & Li, J. Preparation, characterization of PPS micro-porous membranes and their excellent performance in vacuum membrane distillation. *J. Membr. Sci.* **556**, 107–117 (2018).
18. Li, H. et al. Improved desalination properties of hydrophobic GO-incorporated PVDF electrospun nanofibrous composites for vacuum membrane distillation. *Sep. Purif. Technol.* **230**, 115889 (2020).

19. Zhu, H. et al. Preparation and properties of PTFE hollow fiber membranes for desalination through vacuum membrane distillation. *J. Membr. Sci.* **446**, 145–153 (2013).
20. Huang, C. et al. A simple coating method to prepare superhydrophobic layers on ceramic alumina for vacuum membrane distillation. *Sep. Purif. Technol.* **198**, 79–86 (2018).
21. Wang, Y., Zhao, Z., Xi, Z. & Yan, S. Microporous polypropylene membrane prepared via TIPS using environment-friendly binary diluents and its VMD performance. *J. Membr. Sci.* **548**, 332–344 (2018).
22. Tang, N. et al. High permeation flux polypropylene/ethylene vinyl acetate co-blending membranes via thermally induced phase separation for vacuum membrane distillation desalination. *Desalination* **394**, 44–55 (2016).
23. Zhao, L., Wu, C., Liu, Z., Zhang, Q. & Lu, X. Highly porous PVDF hollow fiber membranes for VMD application by applying a simultaneous co-extrusion spinning process. *J. Membr. Sci.* **505**, 82–91 (2016).
24. Zhao, L., Lu, X., Wu, C. & Zhang, Q. Flux enhancement in membrane distillation by incorporating AC particles into PVDF polymer matrix. *J. Membr. Sci.* **500**, 46–54 (2016).
25. Alsalhy, Q. F., Ibrahim, S. S. & Khaleel, S. R. Performance of vacuum poly(propylene) membrane distillation (VMD) for saline water desalination. *Chem. Eng. Process. Process Intensif.* **120**, 68–80 (2017).
26. Zhong, W., Hou, J., Yang, H. & Chen, V. Superhydrophobic membranes via facile bio-inspired mineralization for vacuum membrane distillation. *J. Membr. Sci.* **540**, 98–107 (2017).
27. Li, K. et al. Electrothermal hollow fiber membrane for convenient heat management in Joule vacuum membrane distillation. *Chem. Eng. J.* **443**, 136521 (2022).
28. Zhang, H., Li, B., Sun, D., Miao, X. & Gu, Y. SiO2-PDMS-PVDF hollow fiber membrane with high flux for vacuum membrane distillation. *Desalination* **429**, 33–43 (2018).
29. Pan, J. et al. Enhanced anti-wetting and anti-fouling properties of composite PFPE/PVDF membrane in vacuum membrane distillation. *Sep. Purif. Technol.* **282**, 120084 (2022).
30. Tang, Y. et al. Superhydrophobic electrospun FPI/PTFE nanofiber membranes for robust vacuum membrane distillation. *Sep. Purif. Technol.* **326**, 124856 (2023).
31. Zhang, W. et al. Preparation Janus membrane via polytetrafluoroethylene membrane modification for enhanced performance of vacuum membrane distillation desalination. *Sep. Purif. Technol.* **313**, 123465 (2023).
32. Li, Z., Zhang, P., Guan, K., Yoshioka, T. & Matsuyama, H. Water flux enhancement of PVDF membrane by a facile coating method for vacuum membrane distillation. *Desalination* **536**, 115818 (2022).
33. Chen, W. et al. High-flux water desalination with interfacial salt sieving effect in nanoporous carbon composite membranes. *Nat. Nanotechnol.* **13**, 345–350 (2018).
34. Zhao, S. et al. Hydrophilicity gradient in covalent organic frameworks for membrane distillation. *Nat. Mater.* **20**, 1551–1558 (2021).
35. Hu, M., Yu, D. & Wei, J. Thermal conductivity determination of small polymer samples by differential scanning calorimetry. *Polym. Test.* **26**, 333–337 (2007).